A Joint Global Carbon Inversion System Using Both CO_2 and $^{13}CO_2$ Atmospheric Concentration Data

Jing M. Chen[1,2], Gang Mo[2], Feng Deng[2]

[1]International Institute of Earth System Science

Nanjing University

22 Hankou Road, Nanjing, Jiangsu

China, 210093

and

[2]Department of Geography and Program in Planning

University of Toronto

100 St. George Street

Toronto, Ontario, Canada M5S 3G3

(Final version submitted to *Geoscientific Model Development*)

February 2017

Corresponding author: Jing M. Chen, chenj@geog.utoronto.ca

Abstract

21 Observations of $^{13}CO_2$ at 73 sites compiled in the GLOBALVIEW database are used for an

22 additional constraint in a global atmospheric inversion of the surface CO_2 flux using CO_2

23 observations at 210 sites (62 collocated with $^{13}CO_2$ sites) for the 2002-2004 period for 39 land

24 regions and 11 ocean regions. This constraint is implemented using prior CO_2 fluxes estimated with a

25 terrestrial ecosystem model and an ocean model. These models simulate $^{13}CO_2$ discrimination rates

26 of terrestrial photosynthesis and ocean-atmosphere diffusion processes. In both models, the $^{13}CO_2$

27 disequilibrium between fluxes to and from the atmosphere is considered due to the historical change

28 in atmospheric $^{13}CO_2$ concentration. This joint inversion system using both $^{13}CO_2$ and CO_2

29 observations is effectively a double deconvolution system with consideration of the spatial variations

30 of isotopic discrimination and disequilibrium. Compared to the CO_2-only inversion, this $^{13}CO_2$

31 constraint on the inversion considerably reduces the total land carbon sink from 3.40±0.84 to

32 2.53±0.93 Pg C y^{-1} but increases the total oceanic carbon sink from 1.48±0.40 to 2.36 ±0.49 Pg C y^{-1}.

33 This constraint also changes the spatial distribution of the carbon sink. The largest sink increase

34 occurs in Amazon, while the largest source increases are in southern Africa, and Asia, where CO_2

35 data are sparse. Through a case study, in which the spatial distribution of the annual $^{13}CO_2$

36 discrimination rate over land is ignored by treating it as a constant at the global average of -14.1‰,

37 the spatial distribution of the inverted CO_2 flux over land was found to be significantly modified (up

38 to 15% for some regions). The uncertainties in our disequilibrium flux estimation are 8.0 PgC y^{-1} ‰

39 and 12.7 Pg C y^{-1} ‰ for land and ocean, respectively. These uncertainties induced uncertainties of

40 0.47 Pg C y^{-1} and 0.54 Pg C y^{-1} in the inverted CO_2 fluxes for land and ocean, respectively. Our joint

41 inversion system is therefore useful for improving the partitioning between ocean and land sinks and

42 the spatial distribution of the inverted carbon flux.

1. Introduction

Over the last few decades, much progress has been made in estimating the global carbon cycle using different methods (*Houghton et al.*, 2007; *Canadell et al.*, 2007; *Le Quéré et al.*, 2013). In particular, atmospheric CO_2 mole fractions measured near the surface have been used to infer the carbon flux over land and ocean surfaces through atmospheric inversion (*Rödenbeck et al.*, 2003; *Michalak et al.*, 2005; *Peylin et al.*, 2005; *Peters et al.*, 2007). However, the uncertainty in the inferred flux is still very large, mostly because of the insufficient number of observation stations and the error in modeling the atmospheric transport of CO_2 from the surface to the observation stations. To reduce this uncertainty, it would be useful to introduce constraints to the inversion using other gas species that are associated the CO_2 flux.

Measurements of the atmospheric concentration of the stable isotope $^{13}CO_2$ at a number of stations across the globe since 1994 have been compiled in a database (*GLOBALVIEW-CO2C13*, 2009), and the number of extended $^{13}CO_2$ records from January 1994 to January 2009 increased to 76 by 2009. The mole fraction of $^{13}CO_2$ to CO_2 in the atmosphere is about 1.1%, and the CO_2 exchange between the surface and the atmosphere generally induces concurrent $^{13}CO_2$ exchange. However, the proportion of the $^{13}CO_2$ flux relative to the CO_2 flux differs at different locations and different times due to different mechanisms that discriminate against heavier $^{13}CO_2$ molecules in the exchange processes, and therefore the $^{13}CO_2$ concentration measured in the atmosphere contains additional information for the CO_2 flux. This information is useful for differentiating between terrestrial and oceanic CO_2 exchanges with the atmosphere because the terrestrial CO_2 flux experiences much greater discrimination against $^{13}CO_2$ than does the oceanic CO_2 flux (*Tans et al.*, 1990; *Ciais et al.*,

65   1995a; *Francey et al.*, 1995). Observed $^{13}CO_2$ mole fractions can also provide independent

66   information on the net CO_2 exchange over land and ocean because the net carbon flux to the surface

67   discriminates against heavier $^{13}CO_2$ (*Fung et al.*, 1997; *Randerson et al.*, 2002; *Suits et al.*, 2005).

68   The $^{13}CO_2$ observations over the globe, albeit with a limited number of stations, could therefore be

69   used to assist in quantifying the global carbon cycle.

70   In previous studies (*Siegenthaler and Oeschger*, 1987; *Keeling et al.*, 1989a; *Francey et al.*,

71   1995; *Randerson et al.*, 2002), atmospheric $^{13}CO_2$ observations have been used to separate ocean and

72   land CO_2 fluxes through the use of a technique dubbed "double deconvolution", by which the CO_2

73   fluxes of land and ocean are separated (deconvolved) based on different discrimination rates against

74    $^{13}CO_2$ in the atmospheric CO_2 exchange with land and ocean surfaces. This double deconvolution

75   often assumes that the discrimination rates over land and ocean are spatially uniform, although they

76   can be temporally variable. Through forward atmospheric transport modeling, the ocean and land

77   CO_2 fluxes were also separated based on the spatial gradients of the measured $^{13}CO_2$ /CO_2 ratio either

78   globally (*Keeling et al.*, 1989b) or by latitudinal bands (*Ciais et al.*, 1995a). The same $^{13}CO_2$ data

79   have also been used in inverse modeling of the surface CO_2 flux (*Enting et al.*, 1995; *Rayner et al.*,

80   1999; *Rayner et al.*, 2008). *Enting et al.* (1995) pioneered a methodology for inverting annual mean

81   ocean and land CO_2 fluxes from both atmospheric CO_2 and $^{13}CO_2$ concentration data for 12 ocean

82   regions and 8 land ecosystems for the 1986-1987 and 1989-1990 periods. *Rayner et al.* (1999)

83   developed a different methodology to invert monthly CO_2 fluxes for 12 ocean and 14 land regions for

84   the period from 1980 to 1995 from CO_2 observations at 12 stations and $^{13}CO_2$ and O_2/N_2

85   observations at 1 station. *Rayner et al.* (2008) refined their methodology and applied it to the period

86   from 1992 to 2005 using CO_2 at 67 sites and $^{13}CO_2$ at 10 sites. These studies showed the usefulness

87   of the additional information from $^{13}CO_2$ observations in improving the inversion of annual mean and

88 seasonality of the CO_2 flux over land and ocean. In these inversion studies, the discrimination rate for

89 land is either assumed to be a constant (*Enting et al*., 1995; *Rayner et al*., 1999) or allowed to vary

90 with the areal fraction of C4 plant in a region (*Rayner et al*., 2008). These inversions based on the

91 Bayesian principle were also constrained with only simple prior estimates of the terrestrial and

92 oceanic CO_2 and $^{13}CO_2$ fluxes. Since the data density (the numbers of CO_2 and $^{13}CO_2$ observation

93 sites) is low, the assumed discrimination constants and these prior estimates would have considerable

94 influence on the inverted results, as this is clearly demonstrated in *Enting et al*. (1995).

95   Atmospheric CO_2 observations have been extensively used to estimate the carbon flux over

96 ocean and land through inverse modeling using Bayesian synthesis (*Gurnay et al.,* 2002*; Rödenbeck*

97 *et al.,*2003*; Baker et al.,* 2006*; Peylin et al.* 2005) or data assimilation techniques (*Peters et al.,* 2007;

98 *Zhang et al.*, 2014). Atmospheric inversion studies (*Gurnay et al.*, 2003; *Jacobson et al.*, 2007) often

99 produced ocean sinks considerably smaller than those estimated based on observed gradients in

100 dissolved inorganic carbon (DIC) in interior ocean using ocean circulation models (*Steinkamp and*

101 *Gruber*, 2013). Recent estimates for the ocean sink for anthropogenic CO_2 in 2000's based on DIC

102 ranges from 1.6 to 2.6 Pg C y^{-1} (*Park et al*., 2010; *Wanninkhof et al*., 2013; *Landschützer et al.*, 2014;

103 *Majkut et al.*, 2014; *DeVries*, 2014; *Rödenbeck et al.,* 2014) with an uncertainty of about 0.6 Pg C y^{-1},

104 while atmospheric inversion results are not yet reliable enough to be included in a global ocean sink

105 synthesis (*Le Quéré et al*., 2013). The partition between ocean and land fluxes using atmospheric

106 inversion techniques is sensitive to errors in atmospheric transport modeling (*Baker et al.,* 2006*;*

107 *Stephens et al.,* 2007) and prior fluxes for land and ocean used to constrain the inversion (*Zhang et*

108 *al., 2014; Chen et al.,* 2015). It would therefore be highly desirable to use $^{13}CO_2$ observations to

109 constrain this partition in the inversion process. Accurate partition between ocean and land sinks is

110 important in global carbon cycle research because (1) land sinks are still more reliably estimated as

111   the residual of the global carbon budget than those from land-based data (*Le Quéré et al*., 2013) and

112   (2) ocean sink estimates based on DIC in ocean water also suffer from considerable errors due to

113   insufficient DIC observations and in ocean circulation modeling (*DeVries*, 2014).

114   The overall goal of this study is to explore the information content of $^{13}CO_2$ measurements

115   for global CO_2 flux estimation through developing a Bayesian synthesis inversion system that uses

116   both CO_2 and $^{13}CO_2$ observations. This system is effectively a new double de-convolution system

117   with the capacity to consider the spatial variations of the prior carbon flux and all major isotopic

118   parameters including photosynthetic discrimination, respiratory signature, and disequilibrium rate. In

119   this study, this new system is used to achieve the following objectives: (1) to partition between ocean

120   and land sinks with consideration of the spatial distributions of $^{13}CO_2$ isotopic parameters over ocean

121   and land; (2) to evaluate the importance of considering the spatial distributions of the $^{13}CO_2$

122   discrimination rate over land in the inversion of the CO_2 flux, and (3) to assess the impacts of the

123   errors in disequilibrium flux estimation on the flux partition between ocean and land. To achieve

124   these objectives, a terrestrial ecosystem model named the Boreal Ecosystem Productivity Simulator

125   (BEPS) is further developed to simulate the spatial distributions of the $^{13}CO_2$ discrimination and

126   disequilibrium rates over land for use in a global Bayesian synthesis inversion with $^{13}CO_2$ constraint.

127   BEPS is also used to produce CO_2 prior fluxes globally to regularize the inversion.

2. Methodology

2.1 The inversion method

2.1.1   Inversion system

131   The nested inversion system with a focus on North America developed by *Deng et al*. (2007)

132   is adopted in this study. In this system, two of the Transcom regions (*Gurney et al*., 2002) in North

133   America are divided into 30 regions according to ecosystem types and administrative boundaries

134   (Figure 1), in order to reduce spatial aggregation errors in the inversion over North America and to

135   investigate the inverted spatial distribution of the carbon flux against ecosystem model results. This

136   nested region serves the purpose of evaluating the influence of the spatial distribution of isotopic

137   discrimination on the inverted carbon flux at a relatively high resolution. Also shown in Figure 1 are

138   the spatial distributions of 210 CO_2 and 73 $^{13}CO_2$ observation sites selected in this study from the

139   NOAA GLOBALVIEW database. Most $^{13}CO_2$ sites except 11 are collocated with CO_2 sites.

140   **2.1.2   Synthesis Bayesian inversion with CO_2 observations**

141   To estimate the CO_2 flux (**f**), we represent the relationship between CO_2 measurements and

142   the flux from the surface by a linear model:

143   $$\mathbf{c} = \mathbf{G}\mathbf{f} + \mathbf{A}c_0 + \boldsymbol{\varepsilon} \tag{1}$$

144   where $\mathbf{c}_{m\times1}$ is a given vector of m CO_2 concentration observations over space and time (m equals

145   number of stations times number of months, and for CO_2 only inversion, it is 12600, i.e. 210 stations

146   $\times$ 60 months, 2000-2004); $\boldsymbol{\varepsilon}_{m\times1}$ is a random error vector with a zero mean and a covariance matrix

147   $cov(\boldsymbol{\varepsilon}) = \mathbf{R}_{m\times m}$; $\mathbf{G}_{m\times(n-1)}$ is a matrix representing a transport (observation) operator, where n-1 is the

148   number of fluxes to be determined (equals 3000, i.e. 50 regions $\times$ 60 months, 2000-2004); $\mathbf{A}_{m\times1}$ is a

149   unity vector (filled with 1) representing the assumed initial well-mixed atmospheric CO_2

150   concentrations (c_0) before the first month; and $\mathbf{f}_{(n-1)\times1}$ is an unknown vector of monthly carbon

151   fluxes of the 50 regions.

152   Combining matrixes $\mathbf{G}$ and $\mathbf{A}$ as $\mathbf{M}_{m\times n} = (\mathbf{G}, \mathbf{A})$ and vectors $\mathbf{f}$ and c_0 as $\mathbf{s}_{n\times1} = (\mathbf{f}^{\mathbf{T}}, c_0)^{\mathbf{T}}$, eq.

153   (1) can be expressed as

154     $$\mathbf{c} = \mathbf{Ms} + \boldsymbol{\varepsilon} \qquad\qquad\qquad (2)$$

155   The inverse problem of estimating $\mathbf{s}$ from $\mathbf{c}$ is often poorly constrained and a Bayesian

156   approach is used to circumvent this problem. Pre-existing knowledge and models incorporating

157   additional sources of information can be used to provide an initial estimate of $\mathbf{s}$, known as the *a*

158   *priori*, to constrain the inversion. This *a priori* is then updated when it is combined with information

159   from $\mathbf{c}$ measurement to form a posterior estimate of $\mathbf{s}$, known as the *a posteriori*. In Bayesian

160   synthesis inversion (*Tarantola*, 1987), the following objective function is employed in the place of

161   the traditional least square objective function:

162     $$J = \frac{1}{2}(\mathbf{Ms} - \mathbf{c})^{\mathbf{T}}\mathbf{R}^{-1}(\mathbf{Ms} - \mathbf{c}) + \frac{1}{2}(\mathbf{s} - \mathbf{s_p})^{\mathbf{T}}\mathbf{Q}^{-1}(\mathbf{s} - \mathbf{s_p}) \qquad\qquad (3)$$

163   where $\mathbf{s_{p}}_{n\times 1}$ is the *a priori* estimate of $\mathbf{s}$; the covariance matrix $\mathbf{Q}_{n\times n}$ represents the uncertainty in the

164   *a priori* estimate; and $\mathbf{R}_{m\times m}$ is the transport model-data mismatch error covariance. By minimizing

165   this objective function expressed in eq. (3), we obtain the posterior best estimate of $\mathbf{s}$ as [*Enting*,

166   2002]:

167     $$\hat{\mathbf{s}} = (\mathbf{M}^{\mathbf{T}}\mathbf{R}^{-1}\mathbf{M} + \mathbf{Q}^{-1})^{-1}(\mathbf{M}^{\mathbf{T}}\mathbf{R}^{-1}\mathbf{c} + \mathbf{Q}^{-1}\mathbf{s_p}) . \qquad\qquad (4)$$

168   Meanwhile the posterior uncertainty matrix for the posterior flux can be deduced as follows:

169     $$\hat{\mathbf{Q}} = (\mathbf{Q}^{-1} + \mathbf{M}^{\mathbf{T}}\mathbf{R}^{-1}\mathbf{M})^{-1} . \qquad\qquad (5)$$

170

171   Following the methodology of Deng and Chen (2011), the CO_2 concentration matrix $\mathbf{c}$ in the

172   above equations is the residual concentration after subtracting the observed concentration with

173   contributions from fossil fuel emission, biomass burning, the prior ocean flux and the prior

174   biospheric flux (see Section 2.4 for detail). In this way, the values in $\mathbf{s_p}$ are set to zero and the

175   inverted flux $\mathbf{s}$ is considered to be an adjustment to the prior flux that contributes to the pre-

176   subtracted portions of the CO_2 concentration.

2.1.3   Synthesis Bayesian inversion with both CO_2 and $^{13}CO_2$ observations

178   We attempt to use $^{13}CO_2$ observations to provide an additional constraint to the otherwise

179   CO_2-only inversion presented above. This additional constraint is possible on the grounds that air

180    $^{13}CO_2$ concentration is affected differently by carbon fluxes from ocean and land surfaces. Since the

181    $^{13}CO_2$ gas is transported passively in similar ways as CO_2, the same transport matrix $\mathbf{M}$ applies to

182    $^{13}CO_2$ data to associate $^{13}CO_2$ observations with the surface$^{13}CO_2$ flux. This simple treatment of the

183   transport matrix differs from Rayner et al. (2008) who considered the reduced response of observed

184    $^{13}CO_2$ concentrations to surface fluxes with time due to its accumulated exchange with the surface.

185   As we are interested in the net CO_2 flux, the exchanges of both $^{13}CO_2$ and CO_2 with the surface are

186   consistently not included in the M matrix calculation, although this simplification would induce

187   errors in the inverted CO_2 flux when the accumulated exchanges are spatially highly heterogeneous.

188   In order to conduct an inversion using both CO_2 and $^{13}CO_2$ observations, we simply append $^{13}CO_2$-

189   related data to the $\mathbf{c}$, $\mathbf{R}$ and $\mathbf{M}$ matrixes in Eq. (4), while the $\mathbf{s}$ matrix remains unchanged as the

190   purpose of this joint inversion is only to optimize the CO_2 flux. For $\mathbf{c}$ and $\mathbf{R}$, $^{13}CO_2$ observations and

191   their variances are appended directly to the original matrixes for the CO_2 only case, as shown in Eq.

192   6. Similarly, the $\mathbf{M}$ matrix is also extended to consider $^{13}CO_2$ transport, and the relevant elements for

193   the $^{13}CO_2$ observation stations are from the original $\mathbf{M}$ matrix. However these elements are

194   multiplied by the $^{13}CO_2$ discrimination rate over land or ocean for each region and each month in

195   order to relate the CO_2 flux to the temporal variations in the measured air $^{13}CO_2$ composition at each

196 station and each month. The extended **M** is a combination of the corrected **M** matrix appended to the

197 **M** matrix for CO_2 (see below)

$$
\begin{bmatrix}
M_{1,1} & M_{1,2} & \dots \dots & M_{1,n} \\
M_{2,1} & M_{2,2} & \dots \dots & M_{2,n} \\
\dots \dots & & & \\
M_{m,1} & M_{m,2} & \dots \dots & M_{m,n} \\
W_{m+1,1} & W_{m+1,2} & \dots \dots & W_{m+1,n} \\
W_{m+k,1} & W_{m+k,2} & \dots \dots & W_{m+k,n}
\end{bmatrix}
\begin{bmatrix}
s_1 \\
s_2 \\
\\
\\
\\
s_n
\end{bmatrix}
=
\begin{bmatrix}
c_1 \\
c_2 \\
\\
c_m \\
c_{m+1} \\
c_{m+k}
\end{bmatrix}
$$

All available CO_2 data

73 stations' ^{13}C data

198   (6)

199 where c_i is the CO_2 concentration (i=1 to m) and ^{13}C composition (i=m+1 to m+k) in the air from the

200 starting month (i=0); M_{ij} is the transport operator between region-month j (hereafter simply referred

201 as region) and station-month i (hereafter simply referred as station), and $W_{ij} = D_j M_{ij}$, in which D_j is

202 the discrimination rate against $^{13}CO_2$ in the CO_2 flux for region j. In the inversion procedure, the

203 difference in concentration between two consecutive times is equated with the flux during the time

204 interval (one month).

205   In order to calculate D_j and C_i (i=m+1 to m+k) in Eq. 6, some theoretical development is

206 made according to the $^{13}CO_2$ budget equation derived by Tans et al. (1993):

207 $\quad C_a \dfrac{d\delta_a}{dt} = F_f(\delta_f - \delta_a) - (F_{lph} - F_{lb})\varepsilon_{lph} + F_{lb}(\delta_{lb} - \delta_{lb}^e) - (F_{oa} - F_{oa})\varepsilon_{ao} + F_{oa}(\delta_a^e - \delta_a)$ (7)

208 where C_a is the CO_2 pool in the atmosphere (in Pg C), δ_a is the ^{13}C composition of the atmosphere

209 in ‰, F_f is the carbon emission from fossil fuels and biomass burning, δ_f is the ^{13}C composition of

210 fossil fuels or biomass, F_{lph} is the photosynthetic carbon uptake by the land biosphere (always

211 positive), F_{lb} is the respiratory carbon flux of the land biosphere (always positive), ε_{lph} is the

212 photosynthetic discrimination of the land biosphere in ‰, δ_{lb} is the ^{13}C composition of the land

213   respiratory carbon flux (see Section 2.2.2), δ_{lb}^{e} is the biospheric ^{13}C composition in equilibrium with

214   the current atmosphere (i.e. in 2003), F_{oa} is the one-way carbon from the ocean surface to the

215   atmosphere (always positive), F_{ao} is the one-way carbon flux from the atmosphere to the ocean

216   surface (always positive), ε_{ao} is the air-to-ocean fractionation, ε_{oa} is the air-to-ocean fractionation,

217   and δ_{a}^{e} is the ^{13}C composition in equilibrium with the ocean surface. Eq. 7 states that the temporal

218   variation of the measured ^{13}C composition in the atmospheric CO_2 is determined by contributions

219   from the various sources: fossil fuels and biomass burning (term 1 of the right hand side of Eq. 7),

220   net land biosphere carbon uptake (term 2), one-way respiratory flux from the land biosphere (term 3),

221   net carbon flux of the ocean (term 4), and one-way ocean-to-atmosphere flux (term 5). The one-way

222   carbon fluxes from land and ocean surfaces are important sources of ^{13}C because the atmosphere is in

223   isotopic disequilibrium with these surfaces due to the long-term change of the atmospheric ^{13}C

224   composition. Similar to other terms in Eq. 7, these disequilibrium fluxes are also called isofluxes

225   (*Rayner*, 2001).

226   In order to reduce the errors of our inversion system (Eq. 6) that assumes linear relationships

227   between fluxes and concentrations, the contributions of all fluxes, including prior biospheric and

228   ocean fluxes, to the CO_2 concentration are subtracted from the measured CO_2 concentration prior to

229   the inversion (*Deng and Chen*, 2011). Accordingly, the contributions of all ^{13}C sources to the ^{13}C

230   concentration in the atmosphere are also subtracted from the measured ^{13}C concentration. The

231   purpose of the inversion is then to find the residual CO_2 flux, denoted as **S** in Eq. 6. For this purpose,

232   we denote $S_{lN} = -(F_{lph}-F_{lb})$ as the net flux from the land surface to the atmosphere (negative for sinks)

233   and $S_{oN} = -(F_{ao}-F_{oa})$ as the net flux from the ocean surface to the atmosphere (negative for sinks).

234   After taking $S_{lN} = S_{lN}^{P} + S_{l}$ and $S_{oN} = S_{oN}^{P} + S_{o}$, where S_{lN}^{P} and S_{oN}^{P} are the prior net CO_2 fluxes to the

235   land and ocean surfaces, respectively, and S_l and S_o are the residual fluxes to be inverted for the land

236   and ocean surfaces, respectively, Eq. 7 can be rewritten as:

237    $$S_l \varepsilon_{lph} + S_o \varepsilon_{ao} = C_a \frac{d\delta_a}{dt} - [F_f(\delta_f - \delta_a) + S_{lN}^P \varepsilon_{lph} + F_{lb}(\delta_{lb} - \delta_{lb}^e) + S_{oN}^P \varepsilon_{ao} + F_{oa}(\delta_a^e - \delta_a)] \qquad \textbf{(8)}$$

238   Eq. 8 is the theoretical basis for our joint $^{13}C/^{12}C$ inversion as it links the measured ^{13}C composition

239   in the atmosphere to the CO_2 fluxes of the land and ocean surfaces. In the implementation of the joint

240   inversion system (Eq. 6), a transport matrix is used to link a flux in a particular region to the

241   concentration measured at a particular site. We focus on optimizing the net CO_2 flux using both CO_2

242   and $^{13}CO_2$ observations rather than optimizing the one-way fluxes, and therefore the discrimination

243   terms to be optimized are moved to the left-hand side of Eq. 8 and the disequilibrium terms remain

244   on the right-hand side. Based Eq. 8, the regional discrimination D_j in Eq. 6 is therefore defined as:

245    $$\begin{aligned} D_j &= \varepsilon_{lph,j} \quad \text{for land} \\ D_j &= \varepsilon_{ao,j} \quad \text{for ocean} \end{aligned} \qquad (9)$$

246   where $\varepsilon_{lph,j}$ and $\varepsilon_{ao,j}$ are the ^{13}C fractionation ratio for region j for land and ocean fluxes,

247   respectively. In the joint inversion system, we treat S_l and S_o as the state variables and D_j as

248   predetermined parameters that vary in space (region) and time (monthly). It is therefore prerequisite

249   to estimate accurately these parameters as well as other isotopic parameters on the right hand side of

250   Eq. 8.

251   For land regions, BEPS is used to calculate all land variables in Eq. 8, including S_{lN}^P, F_{lb}, ε_{lph},

252   R_{lb}, δ_{lb} and δ_{lb}^e for each region and month. For ocean regions, ε_{ao}=-2‰, and empirical equations

253   developed by *Ciais et al.* (1995b) are used to calculate F_{oa} and δ_a^e as functions of sea surface

254   temperature on 1°×1° grids.

255   The $^{13}CO_2$ concentration time series (c_{m+1}, ... c_{m+k}) in Eq. 6 in ppm‰ is the numerical

256   realization of the right hand side of Eq. 8 and is computed with the following equation:

257
$$c_i = \overline{C}_{a,i} \frac{d\delta_{a,i}}{dt} - \sum_{k=1}^{5} {}^{13}\delta_k \frac{dC_{k,i}}{dt}$$
(10)

258   In Eq.10, $\overline{C}_{a,i} \frac{d\delta_{a,i}}{dt}$ can be calculated with observed CO_2 concentration and ^{13}C composition at two

259   consecutive times, t and $t+1$, using the following equation:

260
$$\overline{C}_{a,i} \frac{d\delta_{a,i}}{dt} = \frac{C_{a,i}^{t+1} + C_{a,i}^{t}}{2} (\delta_{a,i}^{t+1} - \delta_{a,i}^{t})$$
(11)

261   where $\overline{C}_{a,i}$ is the mean concentration of CO_2 at each observation station i between t and $t+1$, and

262    $\delta_{a,i}$ is the ^{13}C composition at station i, and its derivative with time is taken as its difference between t

263   and $t+1$. This derivative represents the δ_a growth rate that is the combined outcome of the various

264   isofluxes in Eq. 7. The term $\sum_{k=1}^{5} {}^{13}\delta_k \frac{dC_{k,i}}{dt}$ is the sum of $^{13}\delta$ changes due to fossil fuel and biomass

265   burning, prior land ^{13}C discrimination flux, land ^{13}C disequilibrium flux, prior ocean ^{13}C

266   discrimination flux, ocean ^{13}C disequilibrium flux, corresponding to the terms in Eq.8. $^{13}\delta_k$

267   represents $^{13}\delta$ value (‰) for each term in Eq.8, and $\frac{dC_{k,i}}{dt}$ is the change of concentration (ppm)

268   calculated with the flux of each term in Eq.8 according to the atmospheric transport function **M** in

269   Eq.6.

270   The uncertainty of c_i as part of the uncertainty matrix **R** includes the uncertainties of the six

271   terms on the right hand side of Eq. 10. The uncertainty for the first term is based on the measurement

272   error (see next Section 2.1.4) and its global average is 3.08 ppm‰/month. The uncertainties of terms

273   2 to 6 are estimated to be 0.95, 3.17, 0.87, 0.12, and 2.69 ppm‰/month, respectively. The total

274 uncertainty for c_i is therefore 5.33 ppm‰/month as a global average, taking as the square root of the

275 sum of the square of the six uncertainties. As an approximation, this total uncertainty is distributed to

276 each station and each month according to the spatial and temporal patterns of uncertainty of the first

277 term.

278 The inversion system defined by Eq. 6 can be implemented in three ways using (1) CO_2

279 concentration only by excluding the appended matrices for $^{13}CO_2$, (2) $^{13}CO_2$ data only by using

280 $^{13}CO_2$-related matrices only, and (3) both CO_2 and $^{13}CO_2$ data. Through using the data in these three

281 ways, the information content of $^{13}CO_2$ measurements for CO_2 can be systematically investigated.

282 In order to investigate the influences of the isotopic discrimination and disequilibrium over

283 land and ocean on the inversion results, we conduct five sets of inversions for the following cases:

284 Case I: The spatial variations of all isotopic compositions and the discrimination and disequilibrium

285 fluxes in Eq. 8 are considered for both land and ocean. This is the ideal case as the basis to

286 investigate other cases; Case II: The photosynthetic discrimination (ε_{lph}) over land is taken as a

287 constant of -14.1‰, which is the global average obtained by BEPS, and therefore D_j=-14.1‰. This is

288 a case to ignore regional differences in isotopic discrimination over land; Case III: All isotopic

289 variables are the same as Case I, but the land disequilibrium term in Eq. 8 is ignored. This is a case to

290 investigate the influence of the land isotopic disequilibrium on the CO_2 flux inversion; Case IV: All

291 isotopic variables are the same as Case I, but the ocean disequilibrium term in Eq. 8 is ignored. This

292 is a case to investigate the influence of the ocean isotopic disequilibrium on the CO_2 flux inversion;

293 and Case V: Both land and ocean disequilibrium terms are ignored, but all other isotopic variables in

294 Eq. 8 are same as Case I. This is a case to investigate the importance of the total disequilibrium flux

295 in CO_2 flux inversion at the global scale. Cases III to V are useful not only for evaluating the

296 performance of the joint inversion system but also for assessing the impacts of errors in isotopic

297 disequilibrium estimation on the CO_2 flux inversion.

2.1.4 Covariance matrixes for the CO_2 flux and CO_2 and $^{13}CO_2$ concentration measurements

300   In the joint inversion using both CO_2 and $^{13}CO_2$ measurements, the covariance matrix (**Q**) for

301 the CO_2 flux remains the same as that in the CO_2 only inversion (Eq. 3) but the error matrix (**R**) for

302 concentration measurements is expanded to the dimension of 16980×16980 to include 60 months of

303 $^{13}CO_2$ observations at 73 stations. Following *Deng and Chen* (2011), we use an uncertainty of 2.0 Pg

304 C y^{-1} for the total global land surface CO_2 flux, and this total uncertainty is spatially distributed to the

305 39 regions according to the annual total NPP of these regions simulated by BEPS. For each region,

306 the annual total uncertainty is further distributed to each month according to the simulated seasonal

307 variation in NPP. The global total uncertainty (standard deviation) is spatially and temporally

308 distributed in such a way that the total variance is preserved after the distributions, following the

309 principle of TRANSCOM 3 (Gurnay et al., 2003). The uncertainty for the total ocean flux is

310 prescribed as 0.67 Pg C y^{-1} (*Deng and Chen,* 2011). In this way, all the diagonal elements (Q_{ii}) in the

311 uncertainty matrix **Q** are determined, while off-diagonal values are assigned to zero, meaning that no

312 flux covariances between regions and months are assumed. The uncertainty of CO_2 measurements in

313 the **R** matrix is the same as that described in *Deng and Chen* (2011), following the approach of

314 *Peters et al.* (2005) and *Bakers et al.* (2006). In this approach, the uncertainty of a monthly CO_2

315 measurement at a site is estimated as $R_{ii} = \sigma_{const}^2 + GVsd^2$, where constant portion σ_{const} in ppm is

316 assigned according to site category: Antarctic (0.15) , oceanic (0.30), land and tower (1.25),

317 mountain (0.90), and aircraft (0.75), while the site-specific variable portion *GVsd* is obtained from

318 the GLOBALVIEW-CO2 2008 database. The $^{13}CO_2$ measurement uncertainty is calculated in a

319 similar way: the variable portion is obtained from the GLOBALVIEW-13CO2 2008 database, while

320 the constant portion is taken as $R_a \sigma_{const}$ in ppm first, where R_a is the ratio of $^{13}CO_2$ to CO_2 in the air

321 (~0.011147), and then converted to ‰. The average standard deviation of $\delta^{13}C$ observations

322 determined in this way for 73 stations is 0.0685‰.

323

324 **2.2 Prior CO₂ and $^{13}CO_2$ flux estimation**

325 **2.2.1 CO₂ flux**

326 **Terrestrial biosphere fluxes**

327 A process-based terrestrial ecosystem model called the Boreal Ecosystem Productivity Simulator

328 (BEPS) (*Chen et al.*, 1999; *Liu et al.*, 1997) is used in this study to estimate the net terrestrial CO_2

329 flux and its components including the gross primary productivity (GPP), net primary productivity

330 (NPP), heterotrophic respiration (F_{lb}), and net ecosystem productivity (NEP). GPP is calculated using

331 the Farquhar's leaf-level model (*Farquhar et al*, 1980) upscaled to the canopy level using a recently

332 refined two-leaf approach (*Chen et al*., 2012). NPP is taken as 45% of GPP (*Ise et al*., 2010) as

333 global biomass data and its components (stem, foliage, root) are lacking for reliable computation of

334 the autotrophic respiration. F_{lb} is calculated as the sum of the decompositional CO_2 release from 9

335 soil carbon pools, namely coarse and dead wood detritus pool, surface structural pool, surface

336 metabolic pool, surface microbial pool, fine-root structural litter pool, fine-root metabolic pool, soil

337 microbial pool, slow carbon pool, and passive carbon pool. The sizes of these pools for each cover

338 type in each 1° grid are estimated using a model spin-up approach based on simulated NPP in 2000 to

339 create a global land sink of 3.73 Pg C y^{-1}. The total NPP for each 1° grid is taken as a weighted sum

340 of NPP of 7 aggregated land cover types, and the weights are proportional to the areal fractions of the

341 cover types determined using the GLC2000 land cover map at 1 km resolution (*Chen et al.*, 2012).

342 Remotely sensed LAI [*Deng et al.*, 2006] at 1 km resolution and a clumping index map at 6 km

343 resolution (*Chen et al.*, 2005) and a soil textural map (*Webb et al.*, 1991) are aggregated to 1º grids

344 for each cover type based on GLC2000 land cover and used as input to BEPS. National Center of

345 Environmental Prediction (NCEP) reanalyzed data [*Kalnay et al.*, 1996; *Kanamittsu et al.*,2002] are

346 the meteorological drivers for BEPS to simulate hourly carbon fluxes. The output of BEPS used as

347 the prior flux in the inversions is NEP, which does not include carbon emission due to disturbance.

348 **Ocean fluxes**

349   The daily flux of CO_2 across the air-water interface used in this study is constructed based on

350 the results of daily CO_2 fluxes simulated by the OPA-PISCES-T model [*Buitenhuis et al.*, 2006].

351 This model is a global ocean general circulation model (OPA) [*Madec et al.*, 1998] coupled to an

352 ocean biogeochemistry model (PISCES-T) [*Aumont et al.*, 2003; *Buitenhuis et al.*, 2006]. PISCES-T

353 represents the full cycles of C, O_2, P, Si, total alkalinity and a simplified Fe cycle. It also includes a

354 representation of two phytoplankton, two zooplankton and three types of dead organic particles of

355 different sinking rates. OPA-PISCES-T is forced by daily wind stress and heat and water fluxes from

356 the NCEP reanalyzed data [*Kalnay et al.*, 1996, *Kanamittsu et al.*,*2002*]. Hourly S_o (^{13}C) is calculated

357 with gridded optimum interpolation sea surface temperature of NOAA National Climate Data Center

358 (*Reynolds and Smith*, 1994; *Reynolds et al.*, 2002).

359 **Fossil-fuel emissions**

360   The fossil fuel emission field (2000-2004) used in this study (http://carbontraacker.noaa.gov)

361 is constructed based on (1) the global, regional and national fossil-fuel CO_2 emission inventory from

362 1871 to 2006 (CDIAC) [*Marland et al.*, 2009], and (2) the EDGAR 4 database for the global annual

363   CO_2 emission on a 1˚ grid [*Olivier et al.*, 2005]. The $^{13}CO_2$ flux from fossil-fuel consumption is

364   calculated from CO_2 emissions of different fuel types multiplied by their respective $^{13}C/^{12}C$ ratios

365   with consideration of their latitudinal distributions based on *Andres et al.* (2000).

366   **Fire emissions**

367   CO_2 emissions due to vegetation fires are an important part of the carbon cycle [*van der Werf*

368   *et al.*, 2006]. Each year, vegetation fires emitted around or more than 2 PgC of CO_2 into the

369   atmosphere, mostly in the tropics. The fire emission field used in this study is based on the Global

370   Emissions Fire Database version 2 (GFEDv2) (*Randerson et al.*, 2007; *van der Werf et al.*, 2006)

371   **2.2.2 $^{13}CO_2$ flux**

372   Based on the initial work of *Chen et al.* (2006), BEPS is further developed to include a

373   capacity to compute the global distribution of the terrestrial $^{13}CO_2$ flux. Following the principle of

374   multi-stage ^{13}C fractionation in the pathway through leaf boundary layer, stomates, messophyll and

375   chloroplast initially proposed by *Farquhar et al.* (1984, 1989) and implemented globally by *Suits et*

376   *al.* (2005), we developed a module in BEPS for computing the total photosynthetic fractionation and

377   the resultant $^{13}CO_2$ flux. Specifically, the photosynthetic discrimination for C3 plants (Δ_{PC3}) is

378   calculated from

379
$$\Delta_{PC3} = \frac{pA}{C_a}\left[\frac{\Delta_b}{g_b} + \frac{\Delta_s}{g_s} + \frac{\Delta_{diss} + \Delta_{aq}}{g_m}\right] + \frac{C_c}{C_a}\Delta_f \tag{12}$$

380   where Δ_b, Δ_s, Δ_{diss}, Δ_{aq}, and Δ_f are the rates of discrimination against $^{13}CO_2$ through leaf boundary

381   layer, stomates, dissolution in mesophyll water, transport in aqueous phase, and fixation in

382   chloroplast, respectively, and are assigned values of 2.9‰, 4.4‰, 1.1‰, 0.7‰ and 28.2‰,

383   respectively (*Suits et al.*, 2005). A is the photosynthetic rate in mol m^{-2} s^{-1} and p equals to

384      $0.022624T_a/(273.16P)$ with the dimension of m^{3}mol^{-1}, where T_a is air temperature in ºK and P is the

385   standard air pressure at 1.013Bar. C_a and C_c are the CO_2 concentrations in mol mol^{-1} in the free air

386   and leaf chloroplast, respectively. For C4 plants, the photosynthetic discrimination (Δ_{PC4}) is taken as

387   a constant of 4.4‰ (*Suits et al.*, 2005).

388   The leaf boundary-layer (g_b) is calculated with the following equation

389    $$g_b = \frac{\alpha N}{0.5l} \tag{13}$$

390   where α is the diffusivity of CO_2 in dry air in m^{2}s^{-1} calculated as $10^{-6}(0.129+0.007T_a)$ and T_a is the

391   air temperature in °C; l is the leaf characteristic dimension in m, taken as a constant of 0.1 m; and N

392   is the Nusselt number equal to $(u_d l/\upsilon)^{0.5}$, where u_d is the wind speed in m s^{-1}at the vegetation

393   displacement height (80% of the average vegetation height) and υ is the kinematic viscosity of dry air

394   in m^2 s^{-1} calculated as $10^{-6}(0.133+0.007T_a)$. u_d is derived from the wind speed above the canopy

395   based on LAI and vegetation height assigned according to plant functional type (Table 1).

396   As part of the GPP calculation, the stomatal conductance (g_s) computed separately for sunlit

397   and shaded leaves using the Ball-Berry equation (Ball, 1988),

398    $$g_s = f_w(m\frac{A\, h_s}{C_s} p + b) \tag{14}$$

399   where f_w is a scaling factor depending on soil moisture and texture (*Chen et al.*, 2012); h_s is the air

400   humidity at the leaf surface; C_s is the CO_2 concentration at the leaf surface; p is the same as in Eq. 12;

401   and m and b are the slope and intercept in this linear relationship, and they are assigned values

402   according to plant function type (Table 1) (*Chen et al.*, 2012).

403   The mesophyll conductance g_m is calculated based on the method of Harley (1992):

404    $$g_m = \frac{A}{C_i - \dfrac{\Gamma \cdot [J + 8 \cdot (A + R_d)]}{J - 4 \cdot (A + R_d)}} \tag{15}$$

405   where A is the photosynthetic CO_2 assimilation rate; C_i is partial pressure of CO_2 in the air spaces

406   inside leaves; R_d is the respiration rate occurring during the day not related to photorespiration; Γ is

407   the CO_2 compensation point in the absence of R_d; and J is the rate of photosynthetic electron

408   transport. These parameters are the same as those used in computing the CO_2 flux.

409   Our methods of computing stomatal and mesophyll conductances differ from previous studies

410   (*Suits et al*., 2005; *Scholz et al*., 2008; *Rayner et al*., 2008) in the following ways: (1) these

411   conductances are calculated separately for sunlit and shaded leaves because BEPS is a two-leaf

412   model, in which the total GPP of a canopy is taken as the sum of sunlit and shaded leaf GPP; and (2)

413   the mesophyll conductance mechanistically depends on a set of parameters rather than being treated

414   as a constant or to be proportional to the stomatal conductance. Since it has been demonstrated that

415   sunlit and shaded leaf separation is essential for accurate modeling of canopy-level photosynthesis

416   (*Chen et al*., 1999; *Sprintsin et al*., 2011), it is expected that this separation is also essential for $^{13}CO_2$

417   flux estimation. We found that the use of Harley's method for computing the mesophyll conductance

418   makes the calculated ^{13}C photosynthetic fractionation stable for its global application, while the

419   simpler method of treating the mesophyll conductance in proportion with the stomatal conductance

420   often incurs abnormally large or small values of ^{13}C photosynthetic fractionation.

421   The photosynthetic $^{13}CO_2$ flux is in disequilibrium with the respiratory $^{13}CO_2$ flux because of

422   the change in atmospheric $^{13}CO_2$ concentration since the preindustrial time (*Ciais et al*., 1995b; *Fung*

423   *et al*., 1997). The heterotrophic respiratory flux from the decomposition of organic matter of different

424   ages carries the memory of the past atmospheric $^{13}CO_2$ concentration, while the photosynthetic $^{13}CO_2$

425   flux is affected by the current atmospheric $^{13}CO_2$ concentration. The isotopic composition of each of

426   the 9 soil carbon pools ($\delta^{13}C_{soil,\,i}$) is estimated with following formula:

427 $$\delta^{13}C_{soil, i} = \delta^{13}C_a \,(2003 - \tau_i) - \varepsilon_{lph} \tag{16}$$

428   where $\delta^{13}C_a$ is the isotopic composition of carbon in atmosphere CO_2 in the past as determined by the

429   ice-cord record (*Francey et al.*, 1999); ε_{lph} is the annual mean of photosynthetic discrimination in

430   2003; and τ_i is the age of carbon pool i (Table 2) (*Ju et al.*, 2005). In the calculation of the mean age

431   of a carbon pool, we have considered the ages of various carbon pools at the time of entering the pool

432   (*Potter et al., 1993*), so that the mean age is considerably larger than the turnover time determined by

433   the decomposition rate (*Fung et al., 1997*). The mean $\delta^{13}C_{soil}$ is taken as the flux-weighted $\delta^{13}C_{soil,i}$

434   for the 9 carbon pools. The results of $\delta^{13}C_{soil}$ for the globe are shown in Figure 5. The ^{13}C

435   composition of the biosphere δ_{lb} in Eq. 8 is taken as the mean $\delta^{13}C_{soil}$, while the biospheric ^{13}C

436   composition δ_{lb}^{e} in equilibrium with the current atmosphere is taken as δ_{a} - ε_{lph}.

437   The accuracy of the BEPS model in simulating atmospheric $^{13}CO_2$ concentration was

438   previously tested (*Chen et al., 2006; Chen and Chen,* 2007) against measurements over a boreal

439   forest at Fraserdale, Ontario, Canada (49∘52'29.9''N, 81∘34'12.3''W). Flask measurements of $\delta^{13}C_a$

440   were made 40 times in both daytime and nighttime on a tower at a height of 20 m during a 3-day

441   campaign on 21-23 July 1999. BEPS simulated these measurements with RMSE=0.34‰ and r^2=0.76.

442   **2.3 Transport modeling**

443   A transport-only version of the atmospheric chemistry and transport model TM5 (Krol et al.,

444   2003; Krol et al., 2005) is used for CO2 and 13CO2 transport modeling to produce a fully linear

445   operator on these fluxes. The spatial resolution of TM5 is 6°×4° for the globe and 3°×2° for North

446   America, and the atmosphere is divided vertically into 25 layers with 5 layers in the planetary

447   boundary layer. Tracer transport (advection, vertical diffusion, cloud convection) in TM5 is driven

448   by offline meteorological fields taken from the European Centre for Medium Range Weather

449   Forecast (ECMWF) model. All physical parameterizations in TM5 are kept the same as the ECMWF

450   formulation to achieve compatibility between them. The four background fluxes from terrestrial

451   ecosystems, oceans, fossil-fuel burning, and biomass burning are individually inputted to TM5 to

452   calculate the contributions of these fluxes to the atmospheric CO_2 and $^{13}CO_2$ concentrations. Since

453   the main purpose of this study is to develop a joint inversion system, only one transport model is

454   used, the transport matrix $\mathbf{M}$ is assumed to be free of errors.

455   **2.4 CO_2 and $^{13}CO_2$ datasets**

456   Monthly CO_2 and $^{13}CO_2$ concentration data from 2000 to 2004 are compiled from the

457   GLOBALVIEW CO_2 and $^{13}CO_2$ database. Though the GLOBALVIEW database consists of both

458   extrapolated and interpolated data that were created based on the technique devised by *Masarie and*

459   *Tans* [1995], we selected the synchronized and smoothed values of actual observations to compile

460   our concentrations datasets. Only direct measurements of CO2 from the GlobalView dataset are used

461   in our inversion after using a time-frequency weighting scheme (Deng and Chen, 2011). There are

462   5431 monthly data from 209 sites for 42 months used for CO2 (5431 out of 8778, i.e. 209×42), and

463   3066 monthly data from 73 sites for 13CO2 (i.e. 73×42 monthly data). Since the number of 13CO2

464   observation sites is much smaller than that of CO2 sites, all monthly data at 73 sites are used for

465   13CO2, and the missing 13CO2 data are filled with the reference data provided in the same

466   GlobalView dataset. The filled data may have introduced an additional error to the dataset as shown

467   in Figure 15b.

468   To minimize the nonlinear aggregation effects of the large regions (*Pickett-Heaps,* 2007), the

469   contributions of the four background fluxes are subtracted from the above monthly concentrations.

470   So the matrix $\mathbf{c}$ in Eqs. (3) and (4) is expressed as

471          $\mathbf{c} = \mathbf{c}_{obs} - \mathbf{c}_{ff} - \mathbf{c}_{bio} - \mathbf{c}_{ocn} - \mathbf{c}_{fire}$ (17)

472 where $\mathbf{c}_{obs}$ is the monthly CO_2 and $^{13}CO_2$ concentrations obtained from GLOBALVIEW, and $\mathbf{c}_{ff}$,

473 $\mathbf{c}_{bio}$, $\mathbf{c}_{ocn}$, and $\mathbf{c}_{fire}$ are simulated contributions of CO_2 and $^{13}CO_2$ concentrations from the terrestrial

474 biosphere, ocean, fossil-fuel, and fire fluxes, respectively.

475

476 ## 3. Results

477 ### 3.1 Prior CO_2 and $^{13}CO_2$ fluxes

478   Terrestrial ecosystem models integrate many sources of information, including vegetation

479 structure, soil, and meteorology, to estimate carbon exchange of the land surface with the atmosphere.

480 Prior CO_2 and $^{13}CO_2$ fluxes produced by a model can therefore provide indispensible constraints to

481 the otherwise ill-posed inversion based on CO_2 and $^{13}CO_2$ concentration observations alone.

482 Depending on the assigned relative magnitudes of the error matrixes of these observations and these

483 prior fluxes (i.e., **R** and **Q** in Eq. 3), these prior fluxes can have equal or even dominant importance

484 to these observations in the inversion results. We have therefore paid a great attention in modeling

485 these prior fluxes, in order to minimize the total inversion errors. Figure 2a shows an example of the

486 global terrestrial GPP distribution in 2003 modeled by BEPS. The total GPP in this year is 132±22

487 Pg C y^{-1} (*Chen et al*., 2012). This value is larger than some of the recent estimates, such as 123 Pg C

488 y^{-1} by *Beer et al*. (2010), mostly because the LAI values used as input to BEPS are generally larger

489 than those of the MODIS product (*Garrigues et al*., 2008). Our LAI values are larger because we

490 used a global clumping index map derived from a multi-angle satellite sensor POLDER (*Chen et al*.,

491 2005). Clumping increases shaded leaves which contributed about 35% to the total GPP globally.

492 Without considering this clumping effect, the shaded leaf area is underestimated, resulting in an

493 underestimation of the global GPP by 9% (*Chen et al.*, 2012). As the spatial distribution of clumping

494 is not uniform (boreal and tropical forests are most clumped and crops and grasses are least clumped),

495 this refinement in the GPP spatial distribution would have some effects on the inversion results

496 between regions.

497   The net ecosystem productivity (NEP), which is the difference between GPP and ecosystem

498 respiration modeled by BEPS, is shown in Figure 2b for 2003. Even though GPP has a large

499 uncertainty (globally 22 Pg C y^{-1} by BEPS), the uncertainty in NEP is much smaller (globally 2 Pg C

500 y^{-1} by BEPS) because a model spin-up approach is used to estimate the soil carbon pool sizes based

501 on a dynamic equilibrium assumption. Under this assumption, the annual heterotrophic respiration

502 (F_{lb}) equals annual NPP during the preindustrial period, and the soil carbon pool sizes are derived

503 from F_{lb} by solving a set of differential equations describing the decomposition and interactions

504 among the pools (*Govind et al.*, 2011). In this way, F_{lb} is forced to depend on NPP and the systematic

505 biases in GPP are not carried into NEP estimation. NEP is non-zero after the preindustrial period

506 because of the changes in climate and atmospheric composition (CO_2 and nitrogen) as well as

507 disturbance. In our regional modeling, both disturbance and non-disturbance effects are considered

508 for Canada (*Chen et al.*, 2003) and USA (*Zhang et al.*, 2012) forests. However, in our global model

509 spin-up from 1901 (taken as the end of preindustrial period) to 2000, only the non-disturbance effects

510 are considered because of lack of spatially explicit disturbance data outside of North America, while

511 carbon emission due to fire disturbance in the study period from 2000 to 2004 is considered

512 separately using the GFED dataset (*Randerson et al.*, 2007; *van der Werf et al.*, 2006). The prior net

513 CO_2 fluxes for the globe for the years 2002-2004 are given in Table 3 with inversion results with and

514 without the ^{13}C constraint.

515   The global distribution of the total photosynthetic discrimination ($\delta^{13}C_{pt} = \delta^{13}C_a - \Delta$) modeled

516   by BEPS is shown in Figure 3. Forests, such as those in North America, Russia, Europe, Amazon,

517   central Africa, central China and southeast Asia, generally have high photosynthetic discrimination

518   rates (>16‰), while grassland and cropland (in particular C4 grasses and crops) have low

519   discrimination rates. Also shown in Figure 3 is the ocean diffusive discrimination against $^{13}CO_2$. The

520   discrimination over ocean is much smaller than that over land. This difference between land and

521   ocean discrimination may be considered as the largest signal of $^{13}CO_2$ observations on the global

522   carbon cycle (*Tans et al.*, 1990; *Rayner et al.*, 2008) and is considered in our inversion using

523   different $^{13}CO_2$ discrimination rates for ocean and land regions (see Eq. 6).

524   To estimate the disequilibrium between photosynthetic and respiratory discrimination against

525     $^{13}CO_2$, the global distribution of the mean soil carbon age is computed after weighting the ages of the

526   9 soil carbon pools against their fluxes due to decomposition (Figure 4). Forests at high latitudes

527   have the soil carbon age of about 40-60 years, while the tropical forests have much lower values in

528   the range from 10 to 30 years. This latitudinal distribution pattern is mostly determined by soil

529   temperature. In low latitudes, high temperature induces fast turnovers of detritus and fast soil carbon

530   pools, while at high latitudes, low temperature maintains relatively large fractions of slow and

531   passive soil carbon pools. Cropland and grassland also have larger fractions of fast and detritus

532   carbon pools than forest cover types and therefore have younger soil carbon on average. This spatial

533   distribution of soil carbon age has a strong influence on the total respiratory discrimination against

534   ^{13}C ($\delta^{13}C_r$) calculated by BEPS (Figure 5). Respiration from older carbon at high latitudes carries the

535   memory of the older atmosphere with less $^{13}CO_2$ concentration and hence has lower discrimination

536   rates (larger $\delta^{13}C_r$ or smaller absolute value). However, respiration would mostly depend on the

537   photosynthetic discrimination rates as soil organic matter originates from photosynthetic production.

538   As a result, forested areas have higher respiratory discrimination rates (lower $\delta^{13}C_r$ or larger absolute

539   value). Most of the high values of $\delta^{13}C_r$ in Figure 5 are associated with large fractions of C4 plants

540   in the grid, such as the corn belt in the USA, cropland in northeast China, southern border of Sahara

541   desert, and southeast South America. The global distribution of the disequilibrium between

542   photosynthetic and respiratory discrimination, taken as the difference between Figure 3 and Figure 5,

543   is shown in Figure 6. The disequilibrium is the largest at high latitude boreal forests in North

544   America and Eurasia because their soil carbon is the oldest, as shown in Figure 4. The spatial

545   distribution pattern of the disequilibrium is similar to those of *Ciais et al.* (1995b) and *Fung et al.*

546   (1997) but the magnitude is larger because the date of our result in 2000 is more recent than these

547   two previous studies. As the time lapses, the atmosphere is getting lighter in terms of the isotopic

548   composition of CO_2 resulting from the increased air-borne CO_2 from fossil fuel consumption.   Also

549   shown in Figure 6 is the disequilibrium over the ocean estimated using the method of *Ciais et al.*

550   (1995b). This ocean disequilibrium has a large latitudinal gradient because of the gradients in sea

551   surface temperature gradient and the fluxes of CO_2 and $^{13}CO_2$. The spatial distribution in the

552   disequilibrium and the differences in disequilibrium between ocean and land may be considered to be

553   the secondary signal of $^{13}CO_2$ observations on the global carbon cycle. The effects of these

554   disequilibria on the carbon flux are considered in our inversion through presubtracting their

555   contributions to the measured $^{13}CO_2$ composition in Eq. 10.

556   **3.2 Inverse modeling results**

557   Although the inversions were made for the 2000-2004 period, the results of the first two years are not

558   included in the analysis because they are affected by the assumption of uniform global distributions

559 of CO_2 and $^{13}CO_2$ concentrations at the start of our transport modeling using TM5. An 18-24 month

560 period is usually considered to be necessary for the simulated distributions to reach realistic states

561 with reasonably accurate prior surface fluxes from ocean and land and atmospheric transport

562 simulations (*Rödenbeck et al.*, 2003; *Deng and Chen*, 2011). The following results are therefore

563 summarized as the average for the 2002-2004 period.

564 3.2.1 Partition between ocean and land sinks with and without $^{13}CO_2$ constraint

565 To investigate the usefulness of $^{13}CO_2$ observations in partitioning between ocean and land

566 sinks, we conducted inversions with and without $^{13}CO_2$ constraint as expressed in Eq. 6, i.e. with and

567 without the ^{13}C-related expansions of the matrixes. The CO_2-only inversion increases the land sink

568 from the prior of 2.61 PgC y^{-1} to 3.40 PgC y^{-1} while decreasing the ocean sink from the prior of 2.13

569 PgC y^{-1} to 1.48 PgC y^{-1} (Table 3). These results are similar to those of *Deng and Chen* (2011). The

570 results from the joint inversion are considerably different: the posterior sinks for land and ocean

571 become 2.53 and 2.36 PgC y^{-1} (Table 3), respectively, suggesting that the use of $^{13}CO_2$ observations

572 in the inversion considerably influenced the partition between land and ocean fluxes. The ratio

573 between land and ocean sinks is 1.07. The joint inversion system developed in this study may be

574 regarded as a different form of double deconvolution. Using the double deconvolution method with

575 the global average disequilibrium coefficients of 0.49‰ and 0.78‰ and the disequilibrium fluxes of

576 26.8 PgC y^{-1} ‰ and 66 PgC y^{-1} ‰ for land and ocean derived in this study (Table 4), respectively,

577 we also calculated the land and ocean sinks to be 2.90 and 2.36 PgC y^{-1}, respectively. The ratio

578 between land and ocean sinks is 1.23, which is close to the value of 1.07 derived from the joint

579 inversion system, indicating that the joint inversion can effectively perform double deconvolution.

580 Our joint inversion system differs from previous double deconvolution systems (*Siegenthaler and*

581 *Oeschger,* 1987*; Keeling et al.,* 1989a; *Francey et al.*, 1995; *Randerson et al.*, 2002) in the following

582   ways: (1) the estimation of CO_2 fluxes for the land and ocean is additionally constrained by the prior

583   fluxes for the land and ocean rather than entirely dependent on measured CO_2 concentration and

584    $^{13}CO_2$ composition; and (2) the spatio-temporal variations in all parameters associated with isotopic

585   discrimination and disequilibrium are considered in the estimation of the CO_2 flux using a

586   mechanistic biospheric model rather than global average values or simple models based on covariates.

587   These differences in methodology as well as the differences in the mean disequilibrium fluxes may

588   explain why the ocean and land sinks from the joint inversion system differ from the various double

589   deconvolution results.

590   The impacts of $^{13}CO_2$ data on the joint inversion can also be evaluated from the view point of

591   global $^{13}CO_2$ mass budget. Table 5 shows the budgets and its components for the prior, double

592   deconvolution, CO_2-only inversion and joint inversion cases. In these cases, the isofluxes due to

593   fossil fuel emission, land and ocean disequilibrium, and atmospheric storage change are the same,

594   and only those due to discrimination over land and ocean are adjusted. The prior case shows a global

595   imbalance of -5.0 PgC y^{-1} ‰, indicating that either the prior land or ocean fluxes or both are

596   inconsistent with $^{13}CO_2$ measurements. Through double deconvolution, this imbalance is greatly

597   reduced to 0.8 PgC y^{-1} ‰, mostly by an increase in the discrimination flux over land because of its

598   large discrimination rate. The CO_2-only inversion increases the land discrimination flux while

599   decreasing the ocean discrimination flux, resulting in no improvement in the global isotopic balance.

600   The joint inversion optimized both ocean and land fluxes in the direction consistent with $^{13}CO_2$

601   measurements, reducing the imbalance considerably to 1.8 PgC y^{-1} ‰. These cases illustrate clearly

602   that the global isotopic mass balance is very sensitive to the partition between ocean and land fluxes

603   because of the large difference in the discrimination rate between land and ocean. In this analysis, the

604   disequilibrium fluxes are not adjusted, but the influences of the uncertainties in these fluxes on the

605   inversion results are analyzed in Section 3.2.4.

606   Existing estimates for the ocean sink for anthropogenic CO_2 in 2000's varies from 1.94 to 2.6

607   Pg C y^{-1} (*Wanninkhof et al*., 2013; *Landchuster et al.*, 2014; *Majkut et al.*, 2014; *DeVries*, 2014). The

608   average ocean sink for the 2002-2004 period summarized by the Global Carbon Project (GCP) (*Le*

609   *Quéré et al*., 2013) is 2.4 Pg C y^{-1}, while the land sink in the same period is 2.7 Pg C y^{-1} as the

610   residual of the global carbon budget after including the emission due to land use change as a source

611   of carbon. Although the prior estimates of these sinks in our inversions are similar to these values,

612   our CO_2-only inversion considerably increases the land sink and decreases the ocean sink. The

613   addition of $^{13}CO_2$ measurements to the inversion significantly decreases the land sink and increases

614   the ocean sink, pulling the inversion results in the direction to agree with these existing estimates

615   (Figure 7). This may indicate that the use of $^{13}CO_2$ measurements in the joint inversion has improved

616   the CO_2 estimation. In this comparison, we have not considered the unknown small amount (0.1-0.3

617   Pg C y^{-1}) of lateral carbon transport in rivers from land to ocean. This amount is included in some of

618   the estimates of the ocean sink used by GCP, and therefore should be subtracted from the ocean sink

619   and added to the land sink by GCP in order to compare with our atmospheric inversion results.

620   3.2.2 Influence of $^{13}CO_2$ constraint on the spatial distribution of the inverted carbon flux

621   The $^{13}CO_2$ constraint not only modified the partition between ocean and land fluxes but also

622   their spatial distribution patterns. Figure 8 shows the result of the CO_2-only inversion (i.e. without

623   the $^{13}CO_2$ constraint), as the net carbon flux over land and ocean averaged for the period of 2002-

624   2004. Figure 9 shows the difference between inversions with and without the $^{13}CO_2$ constraint, i.e.

625   the result of $CO_2+^{13}CO_2$ inversion minus that of CO_2–only inversion. The general patterns of the

626 inverted carbon flux are similar between these two inversions because these inversions depend

627 primarily on the CO_2 concentration, the prior flux, the error matrixes of the prior flux, and

628 concentration observations. However, there are several large or notable differences: (1) The Amazon

629 region (Region 31) is changed from a carbon source to a sink (Figure 10. Note: a reduction in sources

630 is shown as a negative value); (2) the carbon sink in the tropical Asia (Region 37) is noticeably

631 reduced (by about 10-20 gC m^{-2}y^{-1} from a sink magnitude of about 80-100 gC m^{-2}y^{-1}); (3) The sink in

632 Asia (Region 36) decreases pronouncedly by about 10-20 gC m^{-2}y^{-1}, while the sinks in Russia

633 (Region 35) and Europe (Region 39) are also reduced by some extents (about 5-20 gC m^{-2}y^{-1}); (4)

634 most small regions in the southern part of North America show increases in sinks, but those in the

635 northern part (Canada and Alaska) show increases in sources (see also Figure 11). The overall sink

636 in North America decreases from 0.67 to 0.54 Pg C y^{-1} (Figure 10); and (5) most ocean regions at

637 mid-latitudes have small gains in sink.

638   It is of particular importance to note that the $^{13}CO_2$ constraint changed the Amazon region

639 from a carbon source of 0.43 ± 0.46 Pg C y^{-1} to a carbon sink of 0.08 ± 0.38 Pg C y^{-1} with a notable

640 reduction in the posterior uncertainty, which is higher than uncertainty reductions in most other

641 regions (Figure 10). This change is likely caused by the relatively large addition of information from

642 $^{13}CO_2$ in this tropical region where CO_2 observations are sparse, causing large uncertainties in the

643 inverted flux in this region in the CO_2-only inversion. *Potter et al.* (2009) simulated the net

644 ecosystem productivity (NEP) of the Amazon region using the CASA model driven by remote

645 sensing inputs and found that the NEP for the region was slightly negative (-0.07 Pg C y^{-1}) over the

646 2000-2004 period. *Davidson et al.* (2012) summarized from various inventory-based studies that

647 mature forests in the region was accumulating carbon at a rate of 0.29-0.57 Pg C y^{-1} over the decade

648 before 2005, meaning that NEP is positive. Since the fire emission is estimated to be 0.50 Pg C y^{-1}

649 (*Richey et al.,* 2002), the Amazon region would be either net source of carbon or about carbon

650 neutral. Since spatially explicit fire emission is considered together with fossil fuel emission as a

651 source in our study, the inverted carbon flux corresponds to –NEP, and therefore the result from our

652 joint inversion is in broad agreement with Potter's and Davidson's results. Without the $^{13}CO_2$

653 constraint, our inversion result shows an unreasonably large source of carbon in the Amazon region.

654 3.2.3 Influence of the spatial distribution of photosynthetic discrimination on the inverted carbon

655 flux

656   The joint inversion results shown in Figures 9 to 11 are from Case I with the best estimates of

657 the ^{13}C discrimination and disequilibrium fluxes and therefore represent a baseline study to which

658 other cases are compared for the purpose of investigating the importance of accurate consideration of

659 the spatial distributions of isotopic discrimination and disequilibrium over land and ocean. Case II is

660 designed to investigate the importance of considering the spatial distribution of the photosynthetic

661 isotopic discrimination over land for inverting the CO_2 flux by fixing the discrimination at a constant

662 over land. Figure 12a shows the spatial distribution of the difference in the total isotopic

663 discrimination, i.e. $D_j = \varepsilon_{lph,j}$, among 39 land regions between Case I and Case II, calculated as Case

664 I minus Case II. Regions with positive differences in D_j are shown with positive differences in the

665 inverted CO_2 flux (Figure 12b), meaning larger sinks (negative values) in Case II, and vice versa.

666 This is because a smaller discrimination rate (smaller than -14.1‰) means a larger CO_2 flux from the

667 atmosphere to the surface (more negative value) for the same change in $^{13}CO_2$ concentration in the

668 atmosphere. Under the same condition, a larger discrimination induces a smaller sink (less negative).

669 The absolute regional differences between Case I and Case II are considerable (Figure 12b), e.g. up

670 to 18 g C m^{-2}y^{-1}, showing increases in sinks in Africa, Asia and Australia and decreases in sinks in

671   Amazon, Europe, Russia and most of the small regions in North America. However, the total global

672   sink values of Case II after ignoring the spatial distribution of the disequilibrium rate over land

673   change very little from those of Case I (Table 3): from 2.53±0.93 to 2.49±0.95 Pg C y^{-1} for land and

674   from 2.36±0.49 to 2.35±0.48 Pg C y^{-1} for ocean. This is because the global mean discrimination rates

675   are the same between these two cases.

676   3.2.4 Influence of the uncertainties in disequilibrium fluxes on the inverted carbon flux

677   The average disequilibrium coefficients and fluxes for land and ocean derived in this study are

678   comparable to published results (Table 4), although the estimates of the disequilibrium flux over

679   ocean in previous studies vary in a large range. The uncertainty in the estimated land and ocean

680   disequilibrium fluxes mainly arises from two sources: the estimated disequilibrium coefficient and

681   one-way CO_2 flux from the surface. Mathematically, the total uncertainty in the disequilibrium flux,

682   denoted as $\Delta(\delta \cdot F)$, equals $\sqrt{(\Delta\delta \cdot F)^2 + (\delta \cdot \Delta F)^2}$. For land, the first source depends on the modeled

683   mean soil carbon age by BEPS, which is estimated to be ±5 years, causing an error in the

684   disequilibrium coefficient to be ±0.11‰ based on the slope of δ_a against time at about 1979 (the

685   flux-weighted global mean soil carbon age is 24 years). The second source is estimated to be 9.5 PgC

686   y^{-1} in NPP, which is taken as 45% of the error in GPP, i.e. 21 PgC y^{-1} (*Chen et al.,* 2012). With

687   NPP=59.4 PgC y^{-1} and the mean disequilibrium efficient of 0.49‰, the uncertainty in the estimated

688   land disequilibrium flux is therefore $\sqrt{(0.11\times59.4)^2 + (0.49\times9.5)^2} = 8.0$ PgC y^{-1} ‰. For ocean, the

689   error in the modeled disequilibrium coefficient is mostly caused by sea surface temperature (SST), if

690   the coefficients in the equation developed by *Ciais et al.* (1995b) are assumed to be accurate. With an

691   error of 1.0K in SST, the error in the calculated global average disequilibrium coefficient is ±0.12‰.

692   The error in one-way the ocean flux is difficult to estimate, but we use the value of 10 PgC y^{-1}

693   inferred from the global isotopic budget uncertainty by *Alden* et al. (2010). Their inferred range of

694   the ocean disequilibrium flux is from 92.3 to100.2 PgC y^{-1} ‰, and we use our disequilibrium

695   coefficient of 0.78‰ to calculate this one-way flux uncertainty. Based on the OPA-PISCES-T model,

696   the one-way flux from ocean to atmosphere is 84.6 PgC y^{-1}, and the uncertainty in the estimated

697   ocean disequilibrium flux is therefore $\sqrt{(0.12 \times 84.6)^2 + (0.78 \times 10)^2} = 12.7$ PgC y^{-1} ‰.

698   Case III, Case IV and Case V are conducted to investigate the relative importance of the

699   disequilibrium fluxes over land and ocean (Table 3) in the CO2 flux inversion. In Case III, where the

700   disequilibrium over land is ignored while other settings remain the same as Case I, the land sink

701   increases by 1.05 PgC y^{-1}, while the ocean sink decreases by 0.08 PgC y^{-1} in comparison with Case I.

702   When the disequilibrium over ocean is ignored instead (Case IV), the land sink increases by 0.13

703   PgC y^{-1}, while the ocean sink increases by 2.08 PgC y^{-1}, in comparison with Case I. When the

704   disequilibria over both land and ocean are ignored, the land sink increases by 1.18 PgC y^{-1}, while the

705   ocean sink increases by 1.96 PgC y^{-1}, in comparison with Case I. Results from these case studies

706   suggest that in the joint inversion using both CO_2 and $^{13}CO_2$ measurements, the inverted CO_2 flux

707   can be significantly influenced by the disequilibrium fluxes of land and ocean. The carbon sinks over

708   land and ocean increase when these disequilibrium fluxes are ignored because the photosynthetic and

709   diffusive sources of $^{13}CO_2$ have to increase to make up for the shortfall due to ignoring the

710   disequilibrium sources. These pronounced influences of the disequilibrium fluxes on the CO_2 sink

711   inversion suggest that $^{13}CO_2$ data contain strong signals for the global carbon cycle. In the joint

712   inversion, these data can have the power to distort the global CO_2 mass balance if the $^{13}CO_2$ mass

713   budget (Eq. 8) is not properly simulated. The influence of $^{13}CO_2$ on the joint inversion depends only

714   weakly on the estimated uncertainty in the $^{13}CO_2$ data. We found that if the uncertainty is reduced by

715 half, the sum of the land and ocean sink deviates from the CO_2-only case by 2-6% for all scenarios,

716 suggesting that the mean disequilibrium fluxes play the dominant roles in the joint inversion.

717   The impacts of these disequilibrium fluxes on the inverted CO_2 flux determined in Case III,

718 Case IV and Case V are similar to previous results using the double deconvolution technique (*Tans et*

719 *al.,* 1993; *Ciais et al.,* 1995b*; Randerson et al.,* 2002). However, the influences of these

720 disequilibrium fluxes on the joint inversion could possibly be compromised due to the small number

721 of ^{13}C observation sites relative to the number of CO_2 observation sites used in the joint inversion.

722 The number of linear equations for CO_2 concentration in our joint inversion system (Eq. 6) greatly

723 exceeds the number for ^{13}C composition, with a potential of dampening the impact of ^{13}C data on the

724 inverted results. To investigate the possibility of this dampening effect, we conducted a set of

725 inversions using ^{13}C data alone (Table 6) and found that the impacts of the disequilibrium fluxes on

726 the inversion results are similar to those of the joint inversion. In Case V shown in Table 6, for

727 example, ignoring the disequilibrium fluxes causes the land sink to increase by 1.06 PgC y^{-1} and

728 ocean sink to increase by 2.37 PgC y^{-1}, resulting in a total increase of 3.43 PgC y^{-1}, which is similar

729 to the total difference of 3.14 PgC y^{-1} produced by the joint inversion. These similar results suggest

730 that ^{13}C data used in the way described by Eqs. 6-8 have played the expected role in the joint

731 inversion. By comparing results shown in Tables 3 and 6, it is also encouraging to see that inversions

732 using ^{13}C data alone can produce reasonable results for the CO_2 flux, although we believe that the

733 joint inversion results shown in Table 3 are more reliable. Our finding on the usefulness of the small

734 $^{13}CO_2$ dataset somewhat confirms the claim of Enting et al. (1993 and 1995) that the temporal trend

735 in $^{13}CO_2$ concentration is the major signal constraining the partition between ocean and land sinks.

736   According to the difference of the inverted flux between Case III to Case I, the uncertainty of

737 8.0 PgC y^{-1} ‰ in the land disequilibrium flux would cause an uncertainty of 0.47 PgC y^{-1} in the land

738 flux. According to the comparison between Case IV to Case I, the uncertainty of 12.7 PgC y^{-1} ‰ in

739 the ocean disequilibrium flux would cause an uncertainty of 0.54 PgC y^{-1} in the ocean flux. These

740 uncertainties in the land and ocean fluxes are 17% and 24% of the jointly inverted fluxes for land and

741 ocean (Case I in Table 3), respectively. The impact of the uncertainty in the disequilibrium flux over

742 land is only slightly smaller than the posterior uncertainty of the inverted land flux, but the impact

743 over ocean is larger than the posterior uncertainty.

744 **Discussion**

745 After the CO_2 fluxes are optimized through the inversions, the posterior CO_2 concentration at

746 all stations in each month can be calculated from Eq. 2, and similarly the posterior $^{13}CO_2$

747 composition can also be calculated from Eq. 10 by replacing the prior discrimination fluxes with

748 posterior discrimination fluxes. One way to evaluate the effectiveness of the joint inversion is to

749 examine the improvement in the posterior CO_2 and $^{13}CO_2$ concentrations against measurements.

750 Figure 13 shows concentrations for 10 randomly selected stations from different regions, which are

751 indicated in Figure 1. The CO_2 and $^{13}CO_2$ concentrations produced using the prior fluxes

752 considerably deviate from observations at all stations. The posterior CO_2 concentration from the

753 CO_2-only inversion shows great improvements over the prior concentration in comparison with

754 observations. The posterior CO_2 concentration from the joint inversion does not differ significantly

755 from that of the CO_2-only inversion. At some stations the joint inversion produces slightly lower root

756 mean square differences (RMSD) against observations, but in some stations the opposite is true, as

757 indicated by the RMSD values shown in the header of each plot. It is expected that in some stations,

758 the posterior CO_2 concentration in the joint inversion can be slightly worsened because of the

759 influence of $^{13}CO_2$. The posterior $^{13}CO_2$ concentration is pronouncedly improved over the prior in

760 comparison with observations and almost mimics the observed magnitudes and temporal variations,

761   indicating that the joint inversion system can forcefully adjust CO_2 fluxes to match with $^{13}CO_2$

762   observation through the prescribed discrimination rates. The posterior CO_2 concentrations for either

763   CO_2-only or joint inversion show larger seasonal amplitudes than observations at northern

764   hemisphere stations, although the means are about the same as observations. This suggests that both

765   carbon uptake during the growing season and ecosystem respiration in the non-growing season might

766   have been overestimated, even though the annual net carbon flux may be unbiased. Further work is

767   needed to constrain the large photosynthetic and respiratory fluxes separately rather than the net flux

768   only.

769   In order to provide a comprehensive evaluation, the posterior CO_2 and $^{13}CO_2$ concentrations at

770   all stations are shown in Figures 14 and 15 against observations. In Figure 14, we see pronounced

771   improvements in the posterior concentrations from both the CO_2-only and joint inversions over the

772   prior case. However, the improvements of these two inversions are similar (the joint inversion has a

773   smaller intercept and a slope closer to one, but the CO_2-only inversion has a slightly larger r^2 value).

774   This is in agreement with the cases shown for the individual stations: some stations are improved and

775   some worsened by the use of $^{13}CO_2$ data, manifesting the force of this additional data on the

776   inversion. In Figure 15, the posterior $^{13}CO_2$ concentration from the joint inversion is shown to be

777   greatly improved from the prior case. In the joint inversion, the increase of the posterior land and

778   ocean sinks over the prior sinks that remove CO_2 from the atmosphere logically corrects for the

779   positive bias in the CO_2 concentration produced using the prior fluxes (Figure 14a). The posterior

780   concentration correlation with observation is stronger for $^{13}CO_2$ than for CO_2, indicating that

781   isofluxes are effectively optimized in the joint inversion according to $^{13}CO_2$ data. However, some

782   points in Figure 15b scatter greatly from the 1:1 line, and these points are mostly likely the missing

783 data filled with the reference data (Section 2.4). As other error sources cannot be excluded, these data

784 are retained in our inversion.

785   After adding $^{13}CO_2$ data to the inversion system, the uncertainty in the inverted CO_2 flux

786 increased from 0.84 to 0.93 PgC y^{-1} for land and from 0.40 to 0.49 PgC y^{-1} for ocean (Table 3,

787 difference between the CO_2-only case and Case I), i.e. 11% and 23% increases in uncertainty for land

788 and ocean, respectively. The relative error in preprocessed $^{13}CO_2$ measurements used in the joint

789 inversion is considerably larger than that in CO_2 measurements, causing these increases in the

790 uncertainty of jointly inverted CO_2 fluxes from the CO_2-only case. The $^{13}CO_2$ measurements were

791 preprocessed before the inversion as the remaining concentration after removing the contributions of

792 fossil fuel emission and prior land and ocean discrimination and disequilibrium fluxes (Eq. 10), and

793 therefore they contain uncertainties from these contributions in addition to measurement

794 uncertainties. Errors in modeling the spatial and temporal variations of the $^{13}CO_2$ flux stem from

795 many sources including errors in modeling the discrimination, which is affected by the fractionation

796 of the $^{13}CO_2$ flow through leaf boundary layer, stomata, mesophyll, etc., and the disequilibrium,

797 which depends on the sizes of 9 soil carbon pools and their ages. Although the ocean $^{13}CO_2$

798 discrimination is small, its disequilibrium has a strong latitudinal gradient, which is approximately

799 calculated using the mean monthly temperature. The error in the calculated ocean disequilibrium

800 coefficient is estimated to be $\pm$1.2‰ for the monthly values at a given location and $\pm$0.12‰ for the

801 global annual total. Because of these errors, we estimate that the relative uncertainty in the prior

802 $^{13}CO_2$ fluxes is similar to that of the prior CO_2 flux over both land and ocean.

803

804 **4. Conclusion**

805   The usefulness of atmospheric $^{13}CO_2$ measurements at 73 stations for global carbon cycle

806   estimation is explored through their use as an additional constraint on an atmospheric inversion of

807   the surface carbon flux using CO_2 observations. The following conclusions are drawn from this

808   study:

809   1. This ^{13}C constraint on the joint inversion considerably alters the partition between land and

810   ocean sinks obtained from CO_2-only inversion, decreasing the land sink from 3.40±0.84 to

811   2.53±0.93 Pg C y^{-1}, while increasing the ocean sink from 1.48±0.40 to 2.36±0.49 Pg C y^{-1} for

812   the 2002-2004 period. Over land, this alteration induces the largest sink increases in the

813   Amazon region and largest source increases in southern Africa and Asia, where CO_2

814   observations are sparse and therefore the additional signal from $^{13}CO_2$ data becomes most

815   important. Over ocean, sink increases are found broadly at middle and high latitudes in both

816   hemispheres.

817   2. The spatial distribution of the $^{13}CO_2$ discrimination rate over land has considerable impacts

818   on the spatial distribution of the inverted CO_2 sink over land (up to 15% in some regions),

819   suggesting that reliable models for simulating the spatial distribution of the ^{13}C discrimination

820   rate over land are needed for effective use of $^{13}CO_2$ data for global carbon cycle inversion.

821   **3.** The joint inversion is sensitive to the $^{13}CO_2$ disequilibrium fluxes over both land and ocean.

822   Ignoring these fluxes in the joint inversion causes the inverted total land and ocean sink to

823   increase by 1.18 and 1.96 PgC y^{-1}, respectively. The uncertainty in our disequilibrium flux

824   calculation is estimated to be 8.0 PgC y^{-1} ‰ and 12.7 Pg C y^{-1} ‰ for land and ocean,

825   respectively, inducing an uncertainty in the inverted flux of 0.47 Pg C y^{-1} for land and 0.54 Pg

826   C y^{-1} for ocean.

Acknowledgement

827

828   We greatly appreciate the GlobalView dataset that is available from the NOAA Climate

829   Monitoring and Diagnostics Laboratory. NCEP/DOE 2 Reanalysis data are provided by the

830   NOAA/OAR/ESRL PSD, Boulder, Colorado, USA, from their Web site at

831   http://www.esrl.noaa.gov/psd/. This research was support by a grant (2010CB950704) from the

832   Global Change Key Program of the Chinese Ministry of Science and Technology and a grant (GR-

833   646) from the former Canadian Foundation for Climate and Atmospheric Sciences. Drs. Misa

834   Ishizawa, Douglas Chan and Kaz Higuchi of Environment Canada (EC) provided useful suggestions

835   and technical assistance at the beginning of the project, and Jonathan Fung assisted in the CO_2-only

836   inversion during his M.Sc. studies. We are also indebted to Drs. Pieter Tans of NOAA and Lin

837   Huang of EC for their guidance in the development and validation of the isotope module in BEPS in

838   the early years. Dr. Peter Rayner was a critical and constructive reviewer of several versions of this

839   paper and provided high-level intellectual inputs to this study which are greatly appreciated.

4. References

841   Alden, C., J. B. Miller, and J. W. C. White (2010), Can bottom-up ocean CO2 fluxes can be
842   reconciled with atmospheric 13C observations?, *Tellus B*, 62B, 369-388.

844   Andres R.J., G. Marland, T. Boden T., and S. Bischof (2000), Carbon dioxide emissions from fossil
845   fuel consumption and cement manufacture, 1751-1991, and an estimate of their isotopic composition
846   and latitudinal distribution, in Wigley T.M.L., Schimel D.S. (eds.) *The Carbon Cycle*. Cambridge:
847   Cambridge University Press. 53-62.

849   Aumont, O., E. Maier-Reimer, S. Blain, and P. Monfray (2003), An ecosystem model of the global
850   ocean including Fe, Si, P colimitations, *Global Biogeochem. Cycles*, *17*(2), 1060.

852   Baker, D. F., R. M. Law, K. R. Gurney, P. Rayner, P. Peylin, A. D. Denning, P. Bousquet, L.
853   Bruhwiler, Y. H. Chen, P. Ciais, I. Y. Fung, M. Heimann, J. John, T. Maki, S. Maksyutov, K.
854   Masarie, M. Prather, B. Pak, S. Taguchi, and Z. Zhu (2006), TransCom 3 inversion intercomparison:
855   Impact of transport model errors on the interannual variability of regional
856   CO2 fluxes, 1988–2003, Global Biogeochem. Cy., 20, GB1002, doi:10.1029/2004GB002439.

857

Ball, J. T. (1988), An analysis of stomatal conductance, Ph.D. thesis, 89 pp., Stanford Univ.,
Stanford, Calif.

Beer, C., M. Reichstein, E. Tomelleri, P. Ciais, M. Jung, N. Carvalhais, C. Rodenbeck, M.A. Arain,
D. Baldocchi, G.B. Bonan, A. Bondeau, A. Cescatti, G. Lasslop, A. Lindroth, M. Lomas, S.
Luyssaert, H. Margolis, K.W. Oleson, O. Roupsard, E. Veenendaal, N. Viovy, C. Williams, F.I.
Woodward, and D. Papale (2010), Terrestrial Gross Carbon Dioxide Uptake: Global Distribution and
Covariation with Climate, *Science* 329:834-838.

Buitenhuis, E., C. Le Quéré, O. Aumont, G. Beaugrand, A. Bunker, A. Hirst, T. Ikeda, T. O'Brien, S.
Piontkovski, and D. Straile (2006), Biogeochemical fluxes through mesozooplankton, *Global
Biogeochem. Cycles*, *20*(2), GB2003.

Canadell, J. G., C. Le Quéré, M. R. Raupach, C. B. Field, E. T. Buitenhuis, P. Ciais, T. J. Conway,
N. P. Gillett, R. A. Houghton, and G. Marland (2007), Contributions to accelerating atmospheric CO_2
growth from economic activity, carbon intensity, and efficiency of natural sinks, *Proceedings of the
National Academy of Sciences*, *104*(47), 18866-18870.

Chen, B., J. M. Chen, P. Tabs and L. Huang (2006), Simulating dynamics of $^{13}CO_2$ in the planetary
boundary layer over a boreal forest region: An approach to estimate carbon isotope rectification.
Tellus 58B, 537-549.

Chen, B., and J. M. Chen, 2007. InterannualTemporal variation in carbon isotope discrimination in
response to meteorological and physiological driving factors in a boreal forest ecosystem, *Plant, Cell
and Environment,* 30: doi: 10.1111/j.1365-3040.2007.01707.

Chen, J. M., J. Liu, J. Cihlar, and M. L. Goulden (1999), Daily canopy photosynthesis model through
temporal and spatial scaling for remote sensing applications, *Ecological Modelling*, *124*(2-3), 99-119.

Chen, J. M., W. Ju, J. Cihlar, D. Price, J. Liu, W. Chen, J. Pan, T. A. Black, and A. Barr (2003),
Spatial distribution of carbon sources and sinks in Canada's forests based on remote sensing, *Tellus B*.
55(2): 622-642.

Chen, J. M., C. H. Menges, and S. G. Leblanc (2005), Global derivation of the vegetation clumping
index from multi-angular satellite data, *Remote Sensing of Environment,* 97: 447-457.

Chen, J. M., G. Mo, J. Pisek, J. Liu, F. Deng, M. Ishizawa, and D. Chan (2012), Effects of foliage
clumping on the estimation of global terrestrial gross primary productivity, *Global Biogeochem.
Cycles*, 26, GB1019, doi:10.1029/2010GB003996.

Chen, J. M., J. Fung, G. Mo, F. Deng, and T. West (2015), Atmospheric inversion of the global
surface carbon flux with consideration of the spatial distribution of US crop production and
consumption. *Biogeosciences,* 12, 323-343.

894

895 Ciais, P., P. P. Tans, M. Trolier, J.W. C. White, and R. J. Francey (1995a). A large northern-
896 hemisphere terrestrial CO2 sink indicated by the 13C/12C ratio of atmospheric CO2. *Science,* 269,
897 1098-1102.

899 Ciais, P., P. P. Tans, J. W. C. White, M. Trolier, R. J. Francey, J. A. Berry, D. R. Randall, P. J.
900 Sellers, J. G. Collatz, and D. S. Schimel (1995b), Partitioning of ocean and land uptake of CO_2 as
901 inferred by $\delta^{13}C$ measurements from the NOAA Climate Monitoring and Diagnostics Laboratory
902 Global Air Sampling Network, *J. Geophys. Res.*, 100(D3), 5051–5070, doi:10.1029/94JD02847.

904 Davidson, E. A., A. C. de Araujo, P. Artaxo et al., (2012), The Amazon basin in transition. *Nature,*
905 481, 321-328.

907 Deng, F., J. M. Chen, M. Ishizawa, C.-W. Yuen, G. Mo, K. A. Z. Higuchi, D. Chan, and S.
908 Maksyutov (2007), Global monthly CO_2 flux inversion with a focus over North America, *Tellus B*,
909 *59*(2), 179-190.

911 Deng, F., J. M. Chen, S. Plummer, M. Chen, and J. Pisek (2006), Algorithm for global leaf area
912 index retrieval using satellite imagery, *IEEE Transactions on Geoscience and Remote Sensing*, *44*(8),
913 2219-2229.

915 Deng, F., and J. M. Chen (2011), Recent global CO_2 flux inferred from atmospheric CO_2
916 observations and its regional analysis. *Biogeosciences,* 8: 3263–3281.
917 DeVries, T. (2014), The oceanic anthropogenic CO2 sink: Storage, air-sea fluxes, and transports over
918 the industrial era, *Global Biogeochem. Cycles*, *28*, 631–647, doi:10.1002/2013GB004739.

920 Enting, I.G., C.M. Trudinger, R.J. Francey and H. Granek (1993), Synthesis inversion of atmospheric
921 CO_2 using the GISS tracer transport model, *Division of Atmospheric Research technical paper,*
922 No.29, CSIRO Australia.

924 Enting, I. G., C. M. Trudinger, and R. J. Francey (1995), A synthesis inversion of the concentration
925 and $\delta^{13}C$ of atmospheric CO_2. *Tellus B*, 47: 35–52.

927 Enting, I. G. (2002), *Inverse Problems in Atmospheric Constituents transport*, Cambridge University
928 Press.

930 Farquhar, G. D., S. von Caemmerer, and J. A. Berry (1980), A biochemical model of photosynthetic
931 CO_2 assimilation in leaves of C3 species, *Planta,* 149, 78–90, doi:10.1007/BF00386231.

933 Farquhar, G. D., and R. A. Richards (1984), Isotopic composition of plant carbon correlates with
934 water-use efficiency of wheat genotypes, *Aust., J. Plant. Physiol*., 11, 539–552.

935 Farquhar G.D., J. R. Ehleringer and K. T. Hubick (1989), Carbon isotope discrimination and
936 photosynthesis. *Annual Review of Plant Physiology and Plant Molecular Biology.* 40:503–537.

937 Francey, R. J., P. P. Tans, C. E. Allison, I. G. Enting, J. W. C. White, and M. Trolier (1995),
938 Changes in oceanic and terrestrial carbon uptake since 1982. *Nature*, 373, 326–330.
939
940 Francey R. J., C. E. Allison, D. M. Etheridge, C. M. Trudinger, I. G. Enting, M. Leuenberger, R. L.
941 Langenfelds, E. Michel, L. P. Steele (1999), A 1000-year high precision record of $\delta^{13}C$ in
942 atmospheric CO_2, *Tellus B*, 51(2), 170–193.
943
944 Fung, I.Y., C. B. Field, J. A. Berry, M. V. Thompson, J. T. Randerson, C. M. Malmström, P. M.
945 Vitousek, G. James Collatz, P. J. Sellers, D. A. Randall, A. S. Denning, F. Badeck (1997), Carbon-
946 13 exchanges between the atmosphere and biosphere, *Global Biogeochemical Cycles,* 11: 507-533.
947 Garrigues S., R. Lacaze, F. Baret, J.T. Morisette, M. Weiss, J.E. Nickeson, R. Fernandes, S.
948 Plummer, N.V. Shabanov, R.B. Myneni, Y. Knyazikhin, W. Yang (2008), Validation and
949 intercomparison of global Leaf Area Index products derived from remote sensing data, *J. Geophys.*
950 *Res*., 113, G02028:doi:10.1029/2007JG000635.
951 GLOBALVIEW-CO2C13: Cooperative Atmospheric Data Integration Project - $\delta^{13}C$ of Carbon
952 Dioxide. CD-ROM, NOAA ESRL, Boulder, Colorado [Also available on Internet via anonymous
953 FTP to ftp.cmdl.noaa.gov, Path: ccg/co2c13/GLOBALVIEW], 2009.
954 Govind, A., and J. M. Chen (2011), Spatially distributed modeling of the long-term carbon balance
955 of a boreal landscape. *Ecological Modeling,* doi:10.1016/j.ecolmodel.2011.04.007.
956 Gurney, K. R., R. M. Law, A. S. Denning, P. J. Rayner, D. Baker, P. Bousquet, L. Bruhwiler, Y. H.
957 Chen, P. Ciais, S.M. Fan, I. Y. Fung, Manuel Gloor, Martin Heimann, K Higuchi, J. John, T Maki, S.
958 Maksyutov, K. Masarie, P. Peylin, M. Prather, B. C. Pak, J. T. Randerson, J. L. Sarmiento, S.
959 Taguchi, T Takahashi, C. W. Yuen (2002), Towards robust regional estimates of CO_2 sources and
960 sinks using atmospheric transport models, *Nature*, *415*(6872), 626-630.
961 Gurney, K. R., K. R. Gurney, R. M. Law, A. S. Denning, P. J. Rayner, D. Baker, P. Bousquet, L.
962 Bruhwiler, Y. H. Chen, P. Ciais, S.M. Fan, I. Y. Fung, M. Gloor, M. Heimann, K. Higuchi, J. John, E.
963 Kowalczyk, T. Maki, S. Maksyutov, P. Peylin, M. Prather, B. C. Pak, J. L. Sarmiento, S. Taguchi, T.
964 Takahashi, C. W. Yuen (2003), TransCom3 CO_2 inversion intercomparison: 1. Annual mean control
965 results and sensitivity to transport and prior flux information, *Tellus B*, *55*(2), 555-579.
966
967 Harley, P. C., F. Loreto, G. Di Marco, and T. D. Sharkey (1992), Theoretical Considerations when
968 Estimating the Mesophyll Conductance to CO_2 Flux by Analysis of the Response of Photosynthesis
969 to CO_2, *Plant Physiol.* 98:1429–1436.
970 Houghton, R.A. (2007), Balancing the global carbon budget, *Annual Review of Earth and Planetary*
971 *Sciences* 35:313-347.
972
973 Ise, T., C. M. Litton, C. P. Giardina, and A. Ito (2010), Comparison of modeling approaches for
974 carbon partitioning: impact on estimates of global net primary production and equilibrium biomass of

woody vegetation from MODIS GPP. *Journal of Geophysical Research*, Vol., 115, G04025, doi:10.1029/2010JG001326.

Jacobson, A., S. Fletcher, N. Gruber, J. Sarmiento, and M. Gloor (2007), A joint atmosphere-ocean inversion for surface fluxes of carbon dioxide: 2. Regional results, *Global Biogeochem. Cycles*, *21*(1), GB1020, doi:10.1029/2006GB002703.

Ju, W., and J. M. Chen (2005), Distribution of soil carbon stocks in Canada's forests and wetland simulated based on drainage class, topography and remote sensing. *Hydrological Processes*, 19:77-94.

Kalnay, E., M. Kanamitsu, R. Kistler, W. Collins, D. Deaven, L. Gandin, M. Iredell, S. Saha, G. White, J. Woollen, Y. Zhu, A. Leetmaa, B. Reynolds, M. Chelliah, W. Ebisuzaki, W. Higgins, J. Janowiak, K. C. Mo, C. Ropelewski, J. Wang, R. Jenne, and D. Joseph (1996), The NCEP/NCAR 40-year reanalysis project, *Bull. Amer. Meteor. Soc.*, *77*, 437-471.

Kanamitsu, M., W. Ebisuzaki, J. Woollen, S-K Yang, J. J. Hnilo, M. Fiorino, and G. L. Potter. (2002), NCEP-DEO AMIP-II Reanalysis (R-2), *Bulletin of the American Meterological Society,* 1631-1643.

Keeling, C. D., R. B. Bacastow, A. F. Carter, S. C. Piper, T. P. Whorf, and co-authors (1989a). A three-dimensional model of atmospheric CO2 transport based on observed winds: 1. analysis of observational data. In: Aspects of climate variability in the Pacific and Western Americas (ed. Peterson, D. H.). American Geophysical Union, Washington, D.C., 165-236.

Keeling, C. D., S. C. Piper, and M. Heimann (1989b). A three-dimensional model of atmospheric CO2 transport based on observed winds: 4. Mean annual gradients and interannual variations. In: Aspects of climate variability in the Pacific and Western Americas (ed. Peterson, D. H.). American Geophysical Union, Washington D.C., 305-363.

Krol, M. C., J. Lelieveld, D. E. Oram, G. A. Sturrock, S. A. Penkett, C. A. M. Brenninkmeijer, V. Gros, J. Williams, and H. A. Scheeren (2003), Continuing emissions of methyl chloroform from Europe, *Nature*, *421*(6919), 131-135.

Krol, M. C., S. Houweling, B. Bregman, M. van den Broek, A. Segers, P. van Velthoven, W. Peters, F. Dentener, and P. Bergamaschi (2005), The two-way nested global chemistry-transport zoom model TM5: algorithm and applications, *Atmos. Chem. Phys.*, *5*(2), 417-432.

Landschützer, P., N. Gruber, D. C. E. Bakker, and U. Schuster, (2014), ecent variability of the global ocean carbon sink. *Global Biogeochemical. Cycles*, *28*, 927–949, doi:10.1002/2014GB004853.

Le Quéré, C, Andres, R. J., Boden, T., Conway, T., Houghton, R. A., House, J. I., Marland, G., Peters, G. P., van der Werf G. R., Ahlstrom, A., Andrew, R. M., Bopp, L., Canadell, J. G., Ciais, P., Doney, S. C., Enright, C., Friedlingstein, P., Huntingford, C., Jain, A. K., Jourdain, C., Kato, E., Keeling, R. F., Klein G. K., Levis, S., Levy, P., Lomas, M., Poulter, B., Raupach, M. R., Schwinger,

1016   J., Sitch, S., Stocker, B. D., Viovy, N., Zaehle. S., and Zeng. N. (2013). The global carbon budget
1017   1959–2011. *Earth Syst. Sci. Data* 5: 165–185, doi:10.5194/essd-5-165-2013.

1018   Liu, J., J. M. Chen, J. Cihlar, and W. M. Park (1997), A process-based boreal ecosystem productivity
1019   simulator using remote sensing inputs, *Remote Sensing of Environment*, *62*(2), 158-175.
1020
1021   Madec, G., P. Delecluse, M. Imbard, and C. Lévy (1998), OPA 8.1 ocean general circulation model
1022   reference manual, *Notes du pôle de modélisation IPSL*, 91pp, http://www.lodyc.jussieu.fr/opa/.
1023
1024   Majkut, J. D., J. L. Sarmiento, and K. B. Rodgers (2014), A growing oceanic carbon uptake: results
1025   from an inversion study of surface pCO2 data. *Global Biogeochemical Cycles*, *28*, 335–351,
1026   doi:10.1002/2013GB004585.
1027
1028   Marland, G., T. A. Boden, and R. J. Andres (2009), Global, Regional, and National Fossil Fuel CO_2
1029   Emissions. In Trends: A Compendium of Data on Global Change. Carbon Dioxide Information
1030   Analysis Center, Oak Ridge National Laboratory, U.S. Department of Energy, Oak Ridge, Tenn.,
1031   U.S.A.
1032
1033   Masarie, K. A., and P. P. Tans (1995), Extension and integration of atmospheric carbon dioxide data
1034   into a globally consistent measurement record, *J. Geophys. Res.*, 100(D6), 11593-11610.
1035
1036   Michalak, A. M., A. Hirsch, L. Bruhwiler, K. R. Gurney, W. Peters, and P. P. Tans (2005),
1037   Maximum likelihood estimation of covariance parameters for Bayesian atmospheric trace gas surface
1038   flux inversions, *J. Geophys. Res.*, 110, D24107, doi:10.1029/2005JD005970.
1039
1040   Olivier, J. G. J., J. A. Van Aardenne, F. J. Dentener, V. Pagliari, L. N. Ganzeveld, and J. A. H. W.
1041   Peters (2005), Recent trends in global greenhouse gas emissions:regional trends 1970–2000 and
1042   spatial distributionof key sources in 2000, *Environmental Sciences*, *2*(2), 81 - 99.
1043
1044   Park, G. H., R. Wanninkhof, S. C. Doney, T. Takahashi, K. Lee, R. A. Feely, C. L. Sabine, J.
1045   Trinanes, and I. D. Lima, (2010), Variability of global net sea-air CO2 fluxes over the last three
1046   decades. Chemical and Physical Meteorology, 62, 352–368.
1047
1048   Patra, P. K., S. Maksyutov, M. Ishizawa, T. Nakazawa, T. Takahashi, and J. Ukita (2005),
1049   Interannual and decadal changes in the sea-air CO_2 flux from atmospheric CO_2 inverse modeling,
1050   *Global Biogeochem. Cycles*, *19*(4), GB4013.

1051   Peters, W., J. B. Miller, J. Whitaker, S. A. Denning, A. Hirsch, M. Krol, D. Zupanski, L. Bruhwiler,
1052   and P. P. Tans (2005), An ensemble data assimilation system to estimate CO2 surface fluxes from
1053   atmospheric trace gas observations, J. Geophys. Res., 110,
1054   D24304, doi:10.1029/2005JD006157.

1055   Peters, W. A. R. Jacobson, C. Sweeney, A. E. Andrews, T.J. Conway, K. Masarie, J. B. Miller, L. M.
1056   P. Bruhwiler, G. Petron, A. I. Hirsch, D. E. J. Worthy, G.R Werf, J. T. Randerson, P. O. Wennberg,
1057   M.C. Krol, P. P. Tans (2007), An atmospheric perspective on North American carbon dioxide
1058   exchange: CarbonTracker, *Proceedings of the National Academy of Sciences*, *104*(48), 18925-18930.

1059 Peylin, P., P. Bousquet, C. Le Quéré, S. Sitch, P. Friedlingstein, G. McKinley, N. Gruber, P. Rayner,
1060 and P. Ciais (2005), Multiple constraints on regional CO_2 flux variations over land and oceans.
1061 *Global Biogeochemical Cycles* 19: doi: 10.1029/2003GB002214.
1062

1063 Pickett-Heaps, C. A. (2007), Atmospheric CO_2 inversion cross-validation using non-surface CO_2
1064 data., *PhD dissertation*.

1065 Potter, C.S., J.T. Randerson, C.B., Field, P.A. Matson, P.M. Vitousek, H.A. Mooney, and S.A.
1066 Klooster (1993), Terrestrial ecosystem production: A process model based on global satellite and
1067 surface data, *Global Biogeochemical Cycles*,7 , 811-841.

1068 Potter, C., S. Klooster, A. Huete, V. Genovese, M. Bustamante, L. Guimaraes Ferreira, R. C. de
1069 Oliveira Jr., and R. Zepp, (2009), Terrestrial carbon sinks in the Brazilian Amazon and Cerrado
1070 region predicted from MODIS satellite data and ecosystem modeling. Biogeosciences, 6, 937–945.
1071

1072 Randerson, J. T., G. J. Collatz, J. E. Fessenden, A. D. Munoz, C. J. Still, J. A. Berry, I. Y. Fung, N.
1073 Suits, and A. S. Denning (2002), A possible global covariance between terrestrial gross primary
1074 production and ^{13}C discrimination: Consequences for the atmospheric ^{13}C budget and its response to
1075 ENSO, *Global Biogeochem. Cycles*, 16(4), 1136, doi:10.1029/2001GB001845
1076

1077 Randerson, J. T., G. R. van der Werf, L. Giglio, G. J. Collatz, and P. S. Kasibhatla (2007), Global
1078 Fire Emissions Database, Version 2 (GFEDv2.1). Data set. , *Available on-line [http://daac.ornl.gov/]*
1079 *from Oak Ridge National Laboratory Distributed Active Archive Center, Oak Ridge, Tennessee,*
1080 *U.S.A.*
1081

1082 Rayner, P. J, 2001. Atmospheric perspectives on the ocean carbon cycle. In E. D. Schulze, S. P.
1083 Harrison, M. Heimann, E. A. Holland, J. Lloyd, I. C. Prentice, and D. Schimel, editors, Global
1084 biogeochemical cycles in the climate system, pages 285–294. Academic Press, San Diego.

1085 Rayner, P. J., I. G. Enting, R. J. Francey, and R. L. Langenfelds (1999), Reconstructing the recent
1086 carbon cycle from atmospheric CO_2, $\delta^{13}C$ and O_2/N_2 observations, Tellus, Ser. B, 51, 213– 232.
1087

1088 Rayner, P. J., R. M. Law, C. E. Allison, R. J. Francey, C. M. Trudinger, and C. Pickett-Heaps (2008),
1089 Interannual variability of the global carbon cycle (1992–2005) inferred by inversion of atmospheric
1090 CO_2 and $\delta^{13}CO_2$ measurements, *Global Biogeochem. Cycles*, 22, GB3008,
1091 doi:10.1029/2007GB003068.

1092 Reynolds, R. W and T. M. Smith (1994), Improved global sea surface temperature analyses using
1093 optimum interpolation. *J. Climate*, 7, 929–948.

1094 Reynolds, R. W., N. A. Rayner, T. M. Smith, D. C. Stokes and W. Wang (2002), An improved in situ
1095 and satellite SST analysis for climate. *J. Climate*, 15, 1609-1625.
1096

1097 Richey, J. E., Melack, J. M., Aufdenkampe, A. K., Ballester, V. M. & Hess, L. L. (2002), Outgassing
1098 from Amazonian rivers and wetlands as a large tropical source of atmospheric CO2. Nature 416,
1099 617–620.
1100
1101 Rödenbeck, C., S. Houweling, M. Gloor, and M. Heimann (2003), CO_2 flux history 1982-2001
1102 inferred from atmospheric data using a global inversion of atmospheric transport, *Atmos. Chem.*
1103 *Phys.*, *3*(6), 1919-1964.
1104 Rödenbeck, C., D. C. E. Bakker, N. Metzl, A. Olsen, C. Sabine, N. Cassar, F. Reum, R. F. Keeling,
1105 and M. Heimann, (2014), Interannual sea–air CO2 flux variability from an observation-driven
1106 ocean mixed-layer scheme, Biogeosciences Discuss., 11, 3167– 3207, doi:10.5194/bgd-11-3167-
1107 2014.
1108
1109 Scholze, M., P. Ciais, and M. Heimann (2008), Modeling terrestrial ^{13}C cycling: Climate, land use
1110 and fire, *Global Biogeochem. Cycles*, 22, GB1009, doi:10.1029/2006GB002899.
1111 Siegenthaler, U. and H. Oeschger (1987). Biospheric CO2 emissions during the past 200 years
1112 reconstructed by deconvolution of ice core data. *Tellus* 39B, 140-154.
1113 Sprintsin, M., J. M. Chen, and P. Czurylowicz (2011), Combining land surface temperature and
1114 shortwave infrared reflectance for early detection of mountain pine beetle infestations in western
1115 Canada. *Journal of Applied Remote Sensing* 5(1), 053566.
1116 Steinkamp, K., and N. Gruber (2013), A joint atmosphere-ocean inversion for the estimation of
1117 seasonal carbon sources and sinks, *Global Biogeochem. Cycles*, *27*, doi:10.1002/gbc.20064.
1118
1119 Stephens, B., et al. (2007), Weak northern and strong tropical land carbon uptake from vertical
1120 profiles of atmospheric CO2, *Science*, *316*(5832), 1732–1735.
1121
1122 Suits, N. S., A. S. Denning, J. A. Berry, C. J. Still, J. Kaduk, J. B. Miller, and I. T. Baker (2005),
1123 Simulation of carbon isotope discrimination of the terrestrial biosphere, *Global Biogeochem. Cycles*,
1124 19, GB1017, doi:10.1029/2003GB002141.
1125
1126 Still, C. J., J. A. Berry, G. J. Collatz, and R. S. DeFries (2003), Global distribution of C3 and C4
1127 vegetation: Carbon cycle implications, *Global Biogeochem. Cycles*, 17(1), 1006, doi: 10.1029 / 2001
1128 GB001807.
1129
1130 Tans, P. P., I. Y. Fung, and T. Takahashi (1990), Observational Contrains on the Global Atmospheric
1131 CO_2 Budget, *Science*, *247*(4949), 1431-1438.
1132
1133 Tans, P. P., J. A. Berry, and R. F. Keeling (1993), Oceanic ^{13}C data: A new window on CO_2 uptake
1134 by the oceans, *Global Biogeochem. Cycles*, 7, 353-368.
1135
1136 Tarantola, A. (1987), *Inverse Problem Theory*, 605 pp., Elsevier, Amsterdam, The Netherlands.
1137

van der Velde, I. R., J. B. Miller, K. Schaefer, K. A. Masarie, S. Denning, J. W. C. White, P. P. Tans, M. C. Krol, and W. Peters (2013), Biosphere model simulations of interannual variability in terrestrial 13C/12C exchange, *Global Biogeochemical Cycles,* 27, 637–649

van der Werf, G. R., J. T. Randerson, L. Giglio, G. J. Collatz, P. S. Kasibhatla, and A. F. Arellano Jr. (2006), Interannual variability of global biomass burning emissions from 1997 to 2004, *Atmos. Chem. Phys. Discuss.*, *6*(2), 3175-3226.

Webb, R. S., C. E. Rosenzweig, and E. R. Levine (1991), A global data set of soil particle size properties, *NASA Tech. Memo.*, TM-4286, 40 pp.

Wanninkhof, R., G. -H. Park, T. Takahashi, C. Sweeney, R. Feely, Y. Nojiri, N. Gruber, S. C. Doney, G. A. McKinley, A. Lenton, C. Le Quéré, C. Heinze, J. Schwinger, H. Graven, and S. Khatiwala, (2013), Global ocean carbon uptake: magnitude, variability and trends, Biogeosciences, 10, 1983-2000, doi:10.5194/bg-10-1983-2013,

Zhang F., J. M. Chen, J. Chen, C. M. Gough, T. A. Martin, D. Dragoni (2012), Evaluating spatial and temporal patterns of MODIS GPP over the conterminous U.S. against flux measurements and a process model, *Remote Sensing of Environment*, Vol. 124: 717-729.

Zhang S.P., X. Yi, X. G. Zheng, Z. Q. Chen, et al., 2014. Global Carbon Assimilation System using a Local Ensemble Kalman Filter with Multiple Ecosystem Models, *Journal of Geophysical Research-Biogeosciences*, doi: 10.1002/2014JG002792.

1163 **Table 1.** Biophysical parameters are assigned by plant functional types in BEPS. References for the

1164 chosen values of these parameters are found in *Chen et al*. (2012).

Parameters[*]	Broadleaf Evergreen	Broadleaf Deciduous	Evergreen Conifers	Deciduous Conifers	Shrub	C4 Plants	Others
V_{cmax} µmol m^{-2} s^{-1} (at 25°C)	29.0±7.7	57.7±21.2	62.5±24.7	39.1±11.7	57.9±19.6	100.7±36.6	90.0±89.5
J_{max} µmol m^{-2} s^{-1}	55.1	123.7	135.2	79.2	124.1	193.1	200.0
N g m^{-2}	2.17±0.8	1.74±0.71	3.10±1.35	1.81±0.64	1.86±0.84	1.62±0.61	1.69±0.69
χ_n m^2 g^{-1}	0.48	0.59	0.33	0.56	0.57	0.62	0.60
Slope (*m*)	8	8	8	8	8	4	8
Intercept (*b*), mol m^{-2} s^{-1}	0.0011	0.0011	0.0011	0.0011	0.0011	0.0011	0.0011
LAI	4.07±2.02	3.14±1.99	3.05±1.62	2.42±1.45	1.49±1.06	1.55±1.22	1.64±1.15
Clumping Index	0.66±0.045	0.70±0.047	0.74±0.057	0.78±0.051	0.75±0.059	0.75±0.050	0.76±0.059
Canopy height (m)	23	23	20	20	4	4	4

1165 Where V_{cmax} is the leaf maximum carboxylation rate at 25°C, J_{max} is the maximum electron transport rate, N is the leaf nitrogen content, χ_n is the slope
1166 of V_{cmax} variation with N, and *m* and *b* are the slope and intercept in the Ball-Berry equation. The peak growing season LAI and clumping index are
1167 given as the mean and standard deviation for each plant functional type.

1168

1169

1170

1171 Table 2. Global average ages of soil carbon pools computed by BEPS with consideration of the

1172 influences of temperature and soil moisture on the decomposition rates of these pools.

1173

1174

Soil carbon pool *i*	Name	Global Average Age τ_i (yr)
1	Surface structural leaf litter	5.0
2	Surface metabolic leaf litter	2.3
3	Soil structural litter	4.4
4	Soil metabolic litter	2.3
5	Woody litter	34.9
6	Surface microbe	11.1
7	Soil microbe	28.5
8	Slow carbon	35.5
9	Passive carbon	667.9

1175
1176

1177 Table 3. Inverted fluxes (Pg C y^{-1}), averaged for 2002 –2004, for land and ocean regions with (CO$_2$ +

1178 ^{13}CO$_2$) and without (CO$_2$ only) ^{13}C constraint. The negative sign denotes the flux from the

1179 atmosphere to the surface (sink). Various treatments are made to ^{13}C discrimination and

1180 disequilibrium fluxes represented by the following cases:

1181 Case I: Full consideration of the regional differences in discrimination and disequilibrium;

1182 Case II: Same as Case I, but the annual photosynthetic discrimination ratio is set at a constant of -

1183 14.1‰, although it's monthly variation pattern as modeled by BEPS is retained;

1184 Case III: Same as Case I, but the disequilibrium flux over land is ignored;

1185 Case IV: Same as Case I, but the disequilibrium flux over ocean is ignored;

1186 Case V: Same as Case I, but the disequilibrium flux over both land and ocean is ignored.

1187

1188

Region	Prior flux	Double De-convolution	Inverted CO$_2$ flux						
			CO$_2$ data	CO$_2$ + ^{13}CO$_2$ data					
				Case I	Case II	Case III	Case IV	Case V	
Land	-2.61 ±2.07	-2.90	-3.40 ±0.84	-2.53 ±0.93	-2.49 ±0.95	-3.58 ±0.93	-2.66 ±0.93	-3.71 ±0.93	
Ocean	-2.13 ±0.67	-2.36	-1.48 ±0.40	-2.36 ±0.49	-2.35 ±0.48	-2.24 ±0.49	-4.44 ±0.49	-4.32 ±0.49	

1189

1190

1191

1192 Table 4. Comparison of land and ocean disequilibrium coefficients and disequilibrium fluxes
1193 calculated in this study with those in previous studies.

1194

1195

Studies	Year	Land Disequilibrium Coefficient (‰)	Land Disequilibrium Flux (PgC y^{-1} ‰)	Ocean Disequilibrium Coefficient (‰)	Ocean Disequilibrium Flux (PgC y^{-1} ‰)
This study	2002-2004	0.49	26.8	0.78	66
Fung et al. (1997)	1988	0.33	N/A	N/A	N/A
Randerson et al. (2002)	1981-1994	0.33	20	0.6	55
Alden et al. (2010)	1991-2007	0.45-0.61	22.7-30.6	N/A	92.3-100.2 (globe total)
Van der Velde et al. (2013)	1991-2007	0.486	25.4	N/A	48.7
Francey et al. (1995)	1987	0.43	25.8	0.48	43.8

1196 Table 5. Global isotopic mass budgets averaged for the 2002-2004 period for the prior, double de-
1197 convolution, CO_2-only inversion, and joint inversion (unit: Pg C y^{-1} ‰). Also shown are ocean and
1198 land net fluxes (unit Pg C y^{-1}) for these cases for comparison purposes. For the prior fluxes, the
1199 component of each flux are indicated in the brackets. The isotopic coefficients are same among the
1200 cases.

Isotopic terms	Prior	Double de-convolution	CO_2 –only inversion	Joint inversion
$-C_a\, d(\delta_a)/dt$	15.0 [750 Pg C×(-0.02‰ y^{-1})]	15.0	15.0	15.0
$F_f\,(\,\delta_f\, - \delta_a)*$	-153.7 [8.9 Pg C y^{-1}×(-17.27‰)]	-153.7	-153.7	-153.7
$-(F_{lph}\, - F_{lb})\varepsilon_{lh}$	36.7 [2.6 Pg C y^{-1}×(-14.10‰)]	40.9	47.9	39.5
$F_{lb}(\delta_{lb}\, - \delta_{lbe})$	26.8 [54.7 Pg C y^{-1}×(-0.49‰)]	26.8	26.8	26.8
$-(F_{ao}\, - F_{oa})\varepsilon_{ao}$	4.2 [2.1 Pg C y^{-1}×(-2.00‰)]	4.8	3.0	4.6
$F_{oa}\,(\delta^e_{oa}\, - \delta_{oa})$	66.0 [84.6 Pg C y^{-1}×(-0.78‰)]	66.0	66.0	66.0
Global Budget	-5.0	0.8	-5.0	1.8
$(F_{lph}\, - F_{lb})$, Pg C y^{-1}	-2.6	-2.9	-3.4	-2.8
$(F_{ao}\, - F_{oa})$, Pg C y^{-1}	-2.1	-2.4	-1.5	-2.3

1201 *F_f is the carbon emission from fossil fuel and biomass burning, 6.9 and 2.1, Pg C y^{-1}, respectively,
1202 and δ_f is weighted average ^{13}C composition for fossil fuel and biomass burning, being 25.27‰, and δ_a=-8.0‰.

1203

1204

1205 Table 6. Inverted fluxes (Pg C y^{-1}), averaged for 2002 –2004, for land and ocean regions using ^{13}C

1206 data only. The negative sign denotes the flux from the atmosphere to the surface (sink). Various

1207 treatments are made to ^{13}C discrimination and disequilibrium fluxes represented by the cases outlined

1208 in Table 3.

1209

Region	Prior flux	Inverted CO$_2$ flux				
		^{13}CO$_2$ data				
		Case I	Case II	Case III	Case IV	Case V
Land	-2.61	-2.60	-2.56	-3.61	-2.65	-3.66
	±2.07	±0.96	±0.99	±0.96	±0.96	±0.96
Ocean	-2.13	-2.28	-2.27	-2.28	-4.65	-4.65
	±0.67	±0.53	±0.54	±0.53	±0.53	±0.53

1210

1211

1212

1213

1214   **Figures**
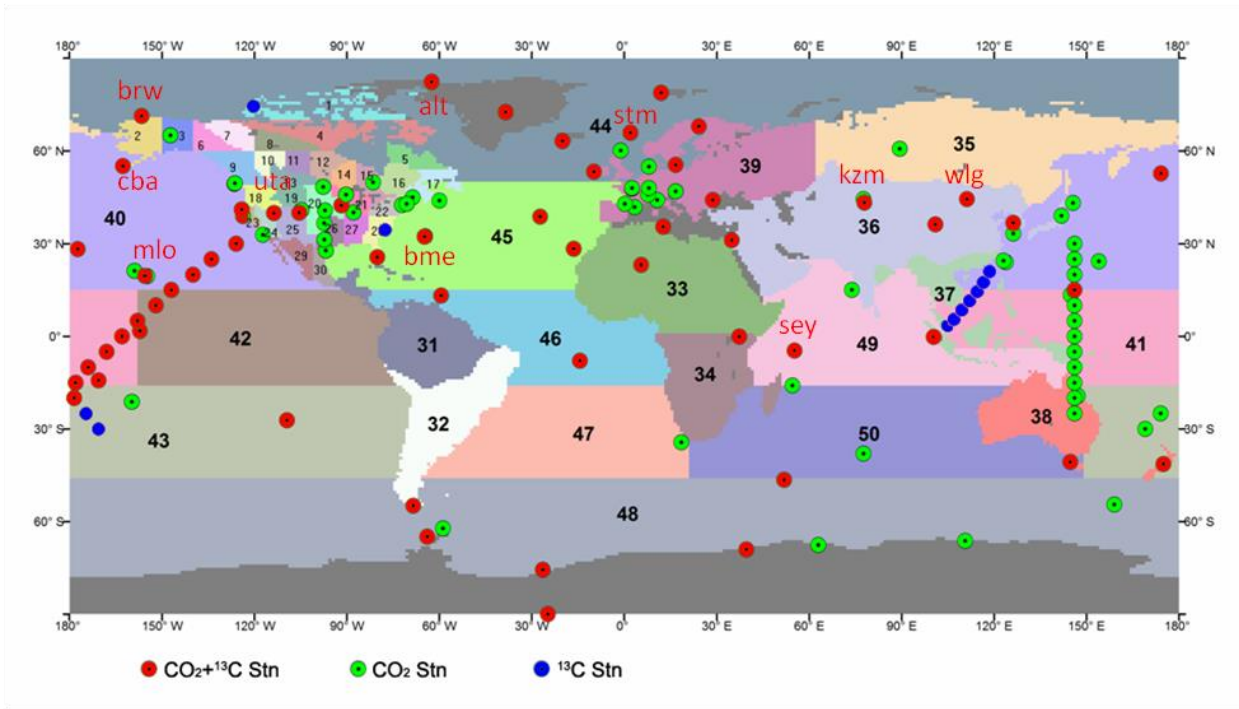
1215

1216   Figure 1. A global nested inversion system with a focus in North America, in which oceans are

1217   divided into 11 regions and land areas are divided into 9 large and 30 small regions outside and

1218   within North America, respectively. Also shown are CO_2 and $^{13}CO_2$ observation stations included in

1219   the GlobalView database and used in this study. 10 of the stations are marked with their names

1220   because they are selected to compare prior and posterior concentrations in Figure 11.

1221

1222

1223

1224

1225
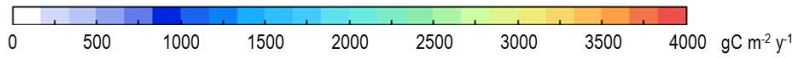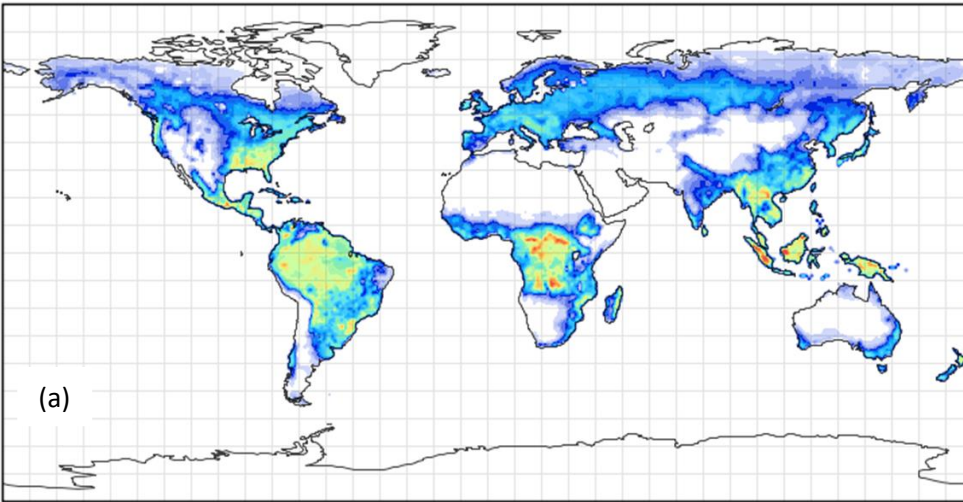
1226
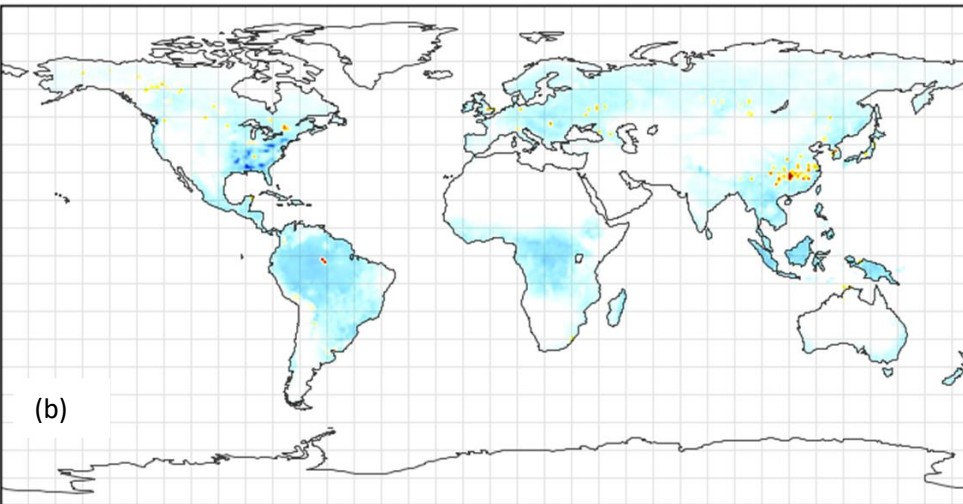
1227

Figure 2. (a) gross primary productivity (GPP) distribution in 2003 computed using remote sensing LAI and land cover maps and climate and soil data, and (b) net ecosystem productivity (NEP) distribution in 2003. Both are calculated using the BEPS model. Annual NEP maps from 2000 to 2004 are used to as the prior flux in the inversions. This GPP map is used to distribute the flux uncertainty among the 39 land regions.
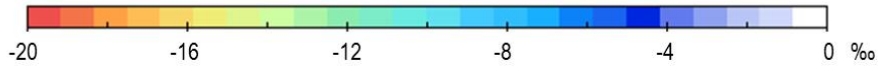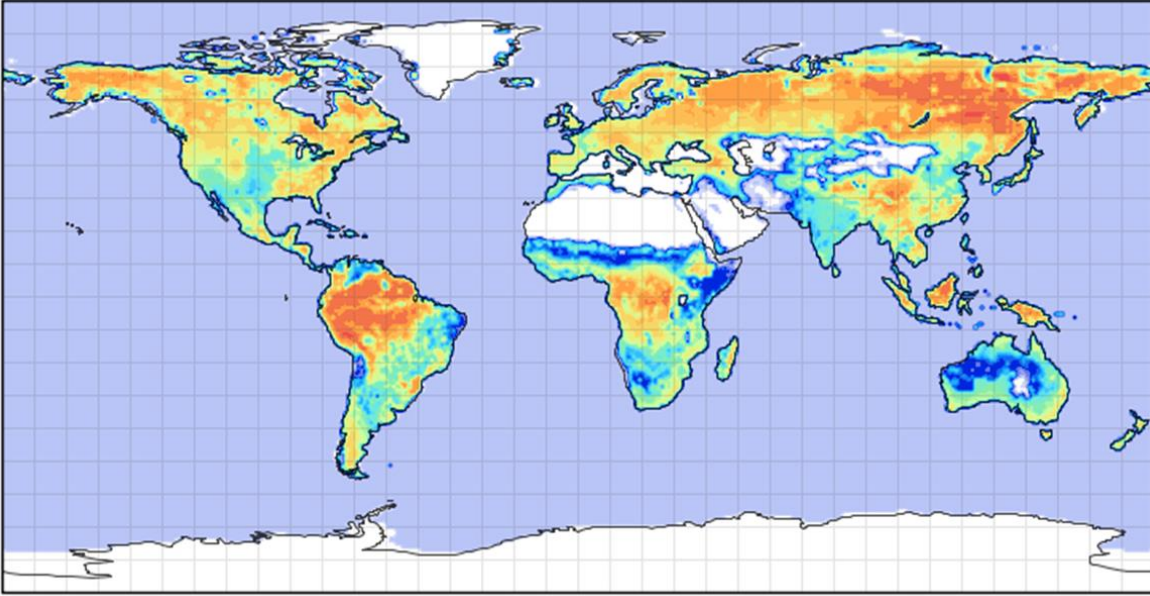
1233

1234   Figure 3. The annual mean of the total photosynthetic ^{13}C discrimination ($\varDelta$ in Eq. 7) in 2003.

1235
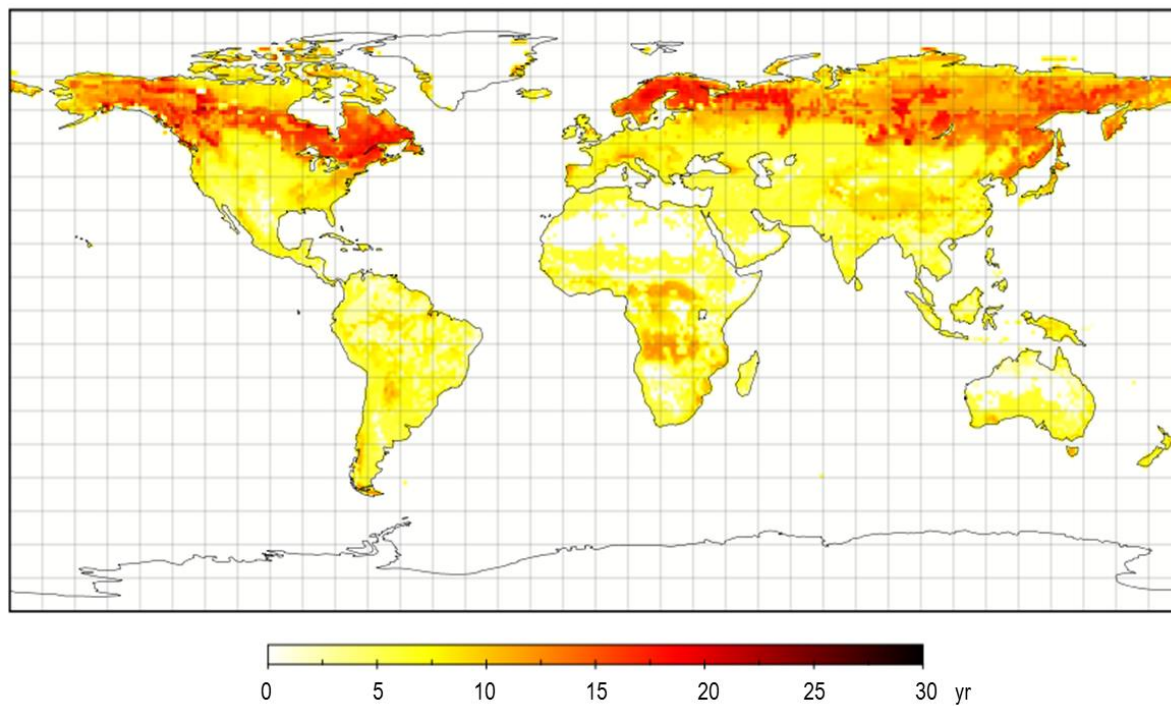
1236

1237   Figure 4. Global distribution of the flux-weighted mean age of soil carbon pools (Eq. 8).

1238

1239

1240

1241
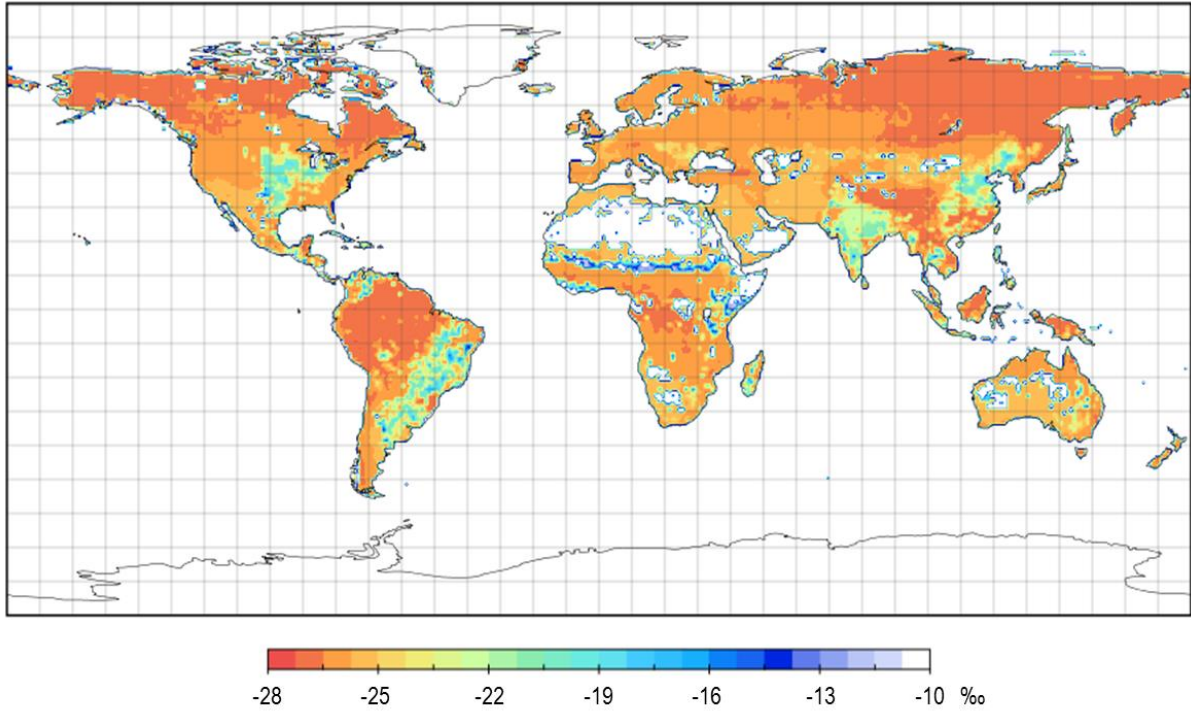
1242

1243   Figure 5. Global $\delta^{13}C$ distribution over land (annual flux-weighted average in 2003).

1244
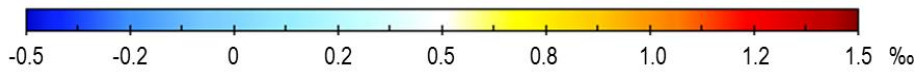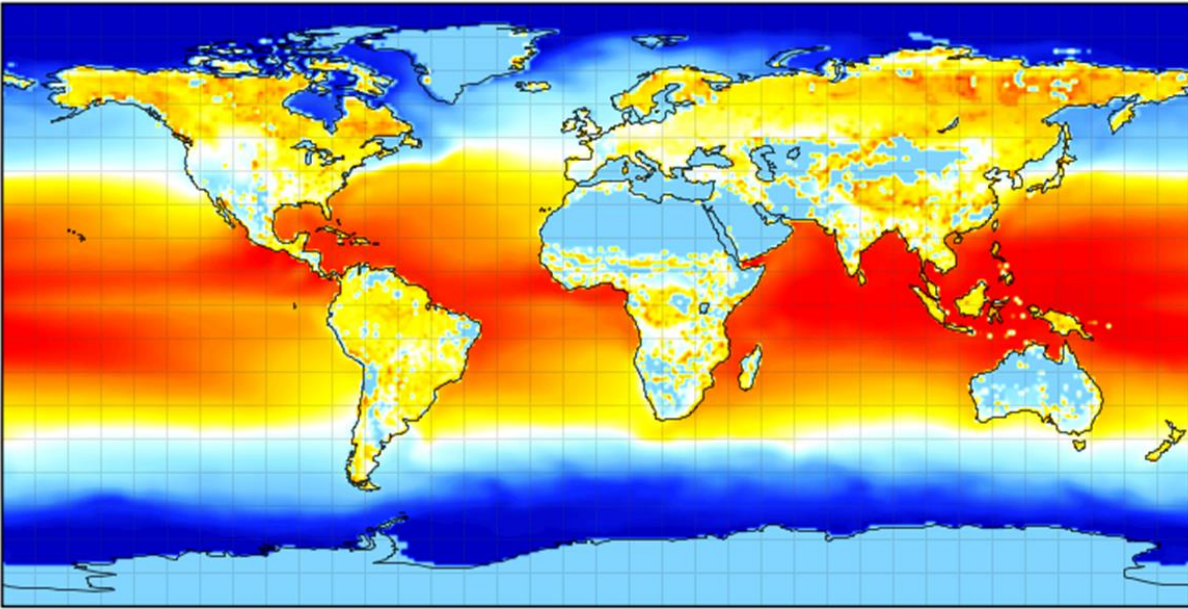
1245

1246

1247 Figure 6. Disequilibria between ^{13}C fluxes to and from the land or ocean surface in 2000. At the land

1248 surface, the disequilibrium is the difference between photosynthetic and respiratory discriminations

1249 against ^{13}C, and at the ocean surface, it is the difference in ^{13}C discrimination between the one-way

1250 diffusive downward and upward fluxes.

1251
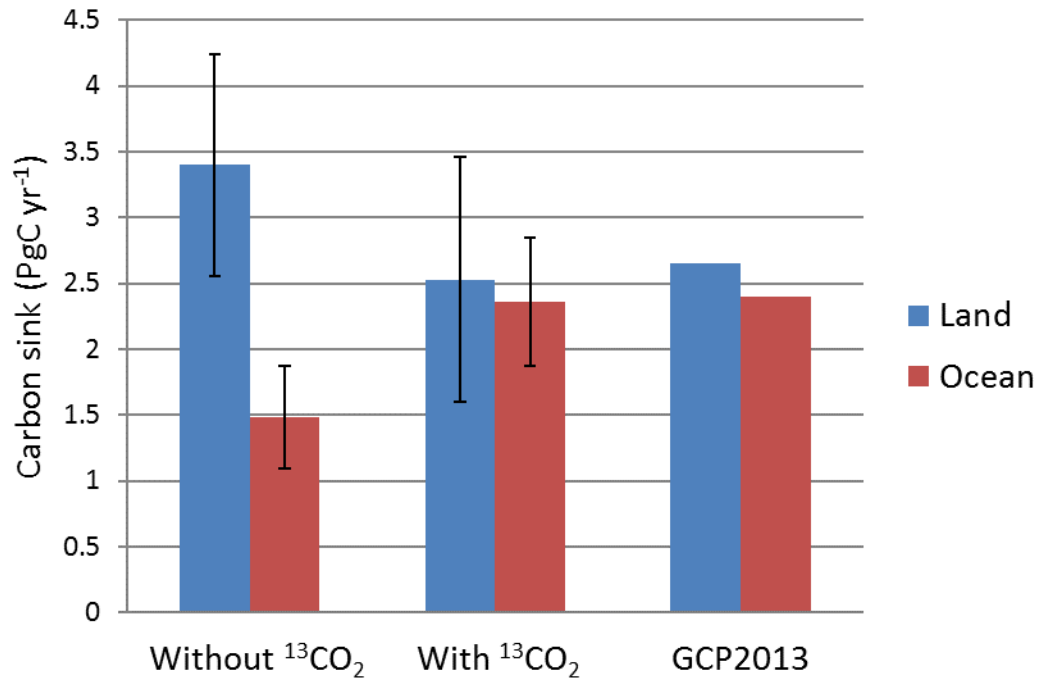
1252

1253   Figure 7. Comparison of land and ocean carbon sinks derived from inversions with and without the

1254 $^{13}CO_2$ constraint against the Global Carbon Project results (*Le Quéré et al.*, 2013).

1255

1256
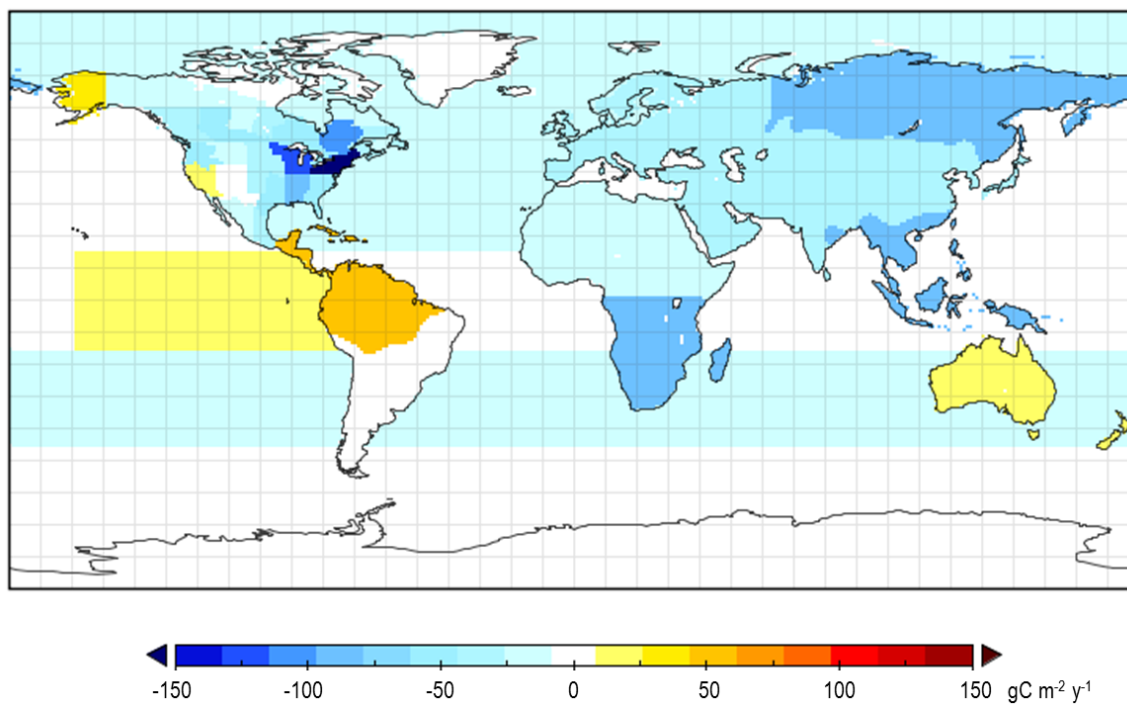
1257

1258   Figure 8. Global distribution of inverted CO_2 flux using CO_2 data only (2002-2004 average).

1259

1260

1261

1262
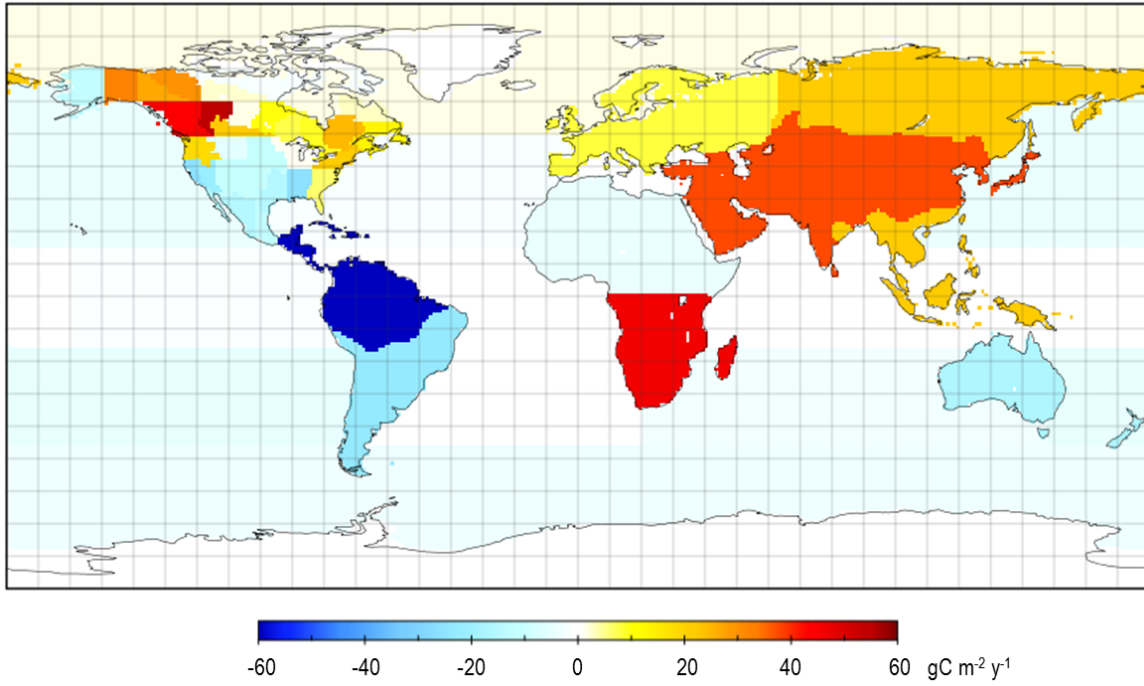
1263

1264   Figure 9. Difference of the inverted CO_2 flux between using $CO_2 + {}^{13}CO_2$ data and using CO_2 data

1265   only (2002-2004 average).

1266

1267

1268

1269

1270

1271

1272

1273

1274
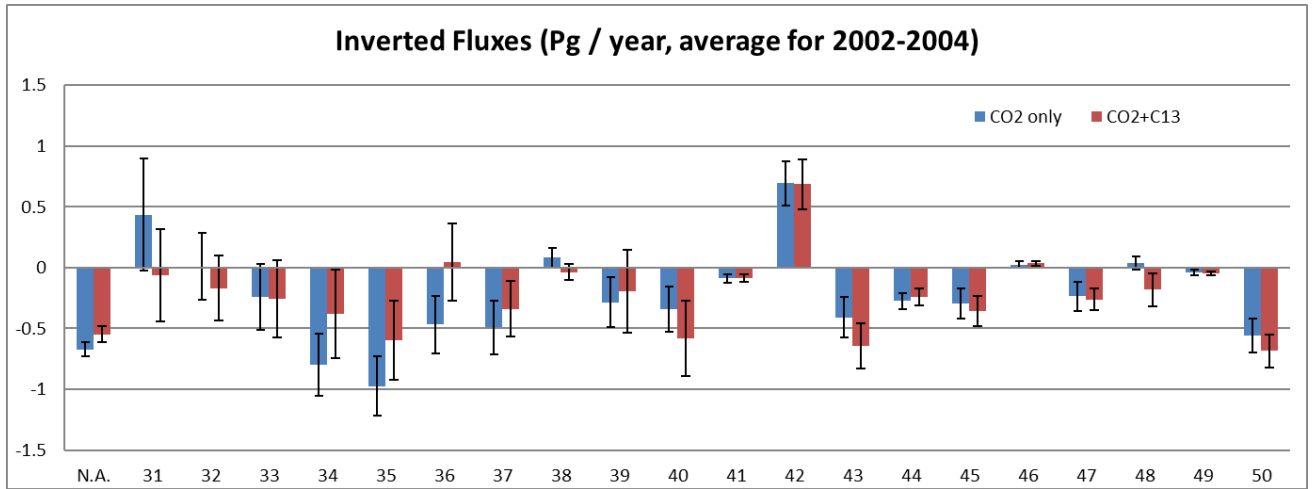
1275

1276 Figure 10. Comparison between inversion results with and without $^{13}CO_2$ constraint for 21 regions of

1277 the globe for the periods of 2002-2004.

1278

1279

1280
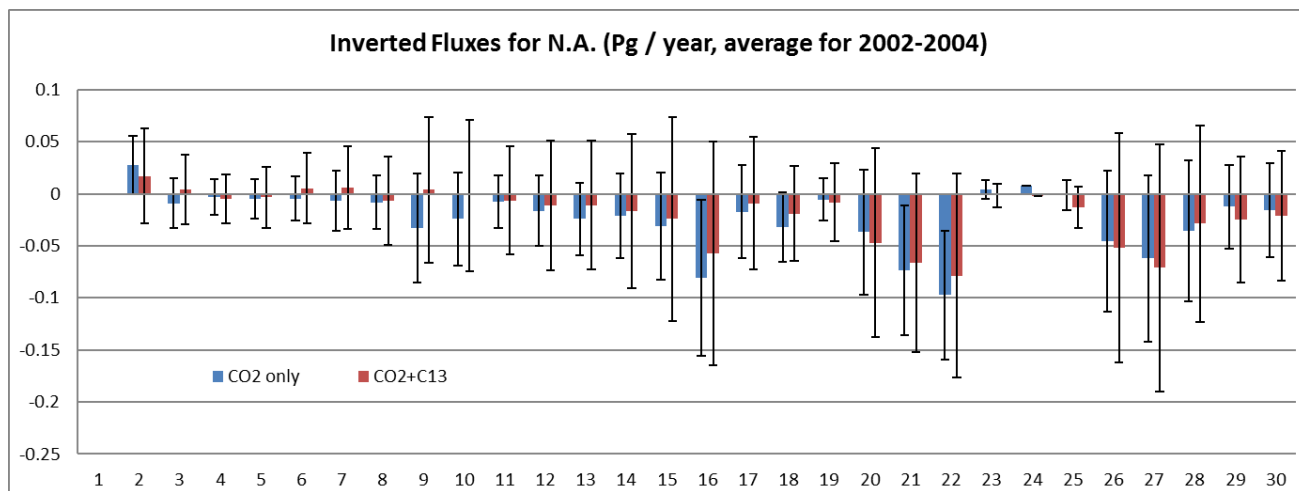
1281

1282   Figure 11. Comparison between inversion results with and without $^{13}CO_2$ constraint for 30 regions in

1283   North America.

1284

1285
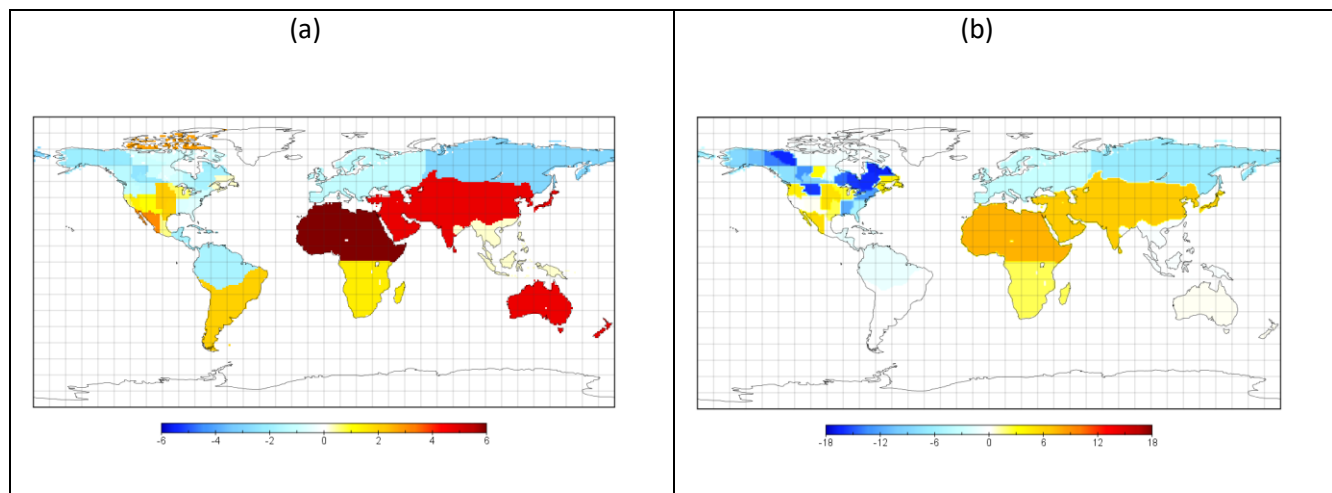
1286

1287 Figure 12. (a) Difference in ε_{lph} (‰) and (b) the inverted CO_2 flux ($gC\ m^{-2}y^{-1}$) between Case I and
1288 Case II, i.e. Case I minus Case II. See Section 2.1.3 for the description of these cases.

1289

1290

1291
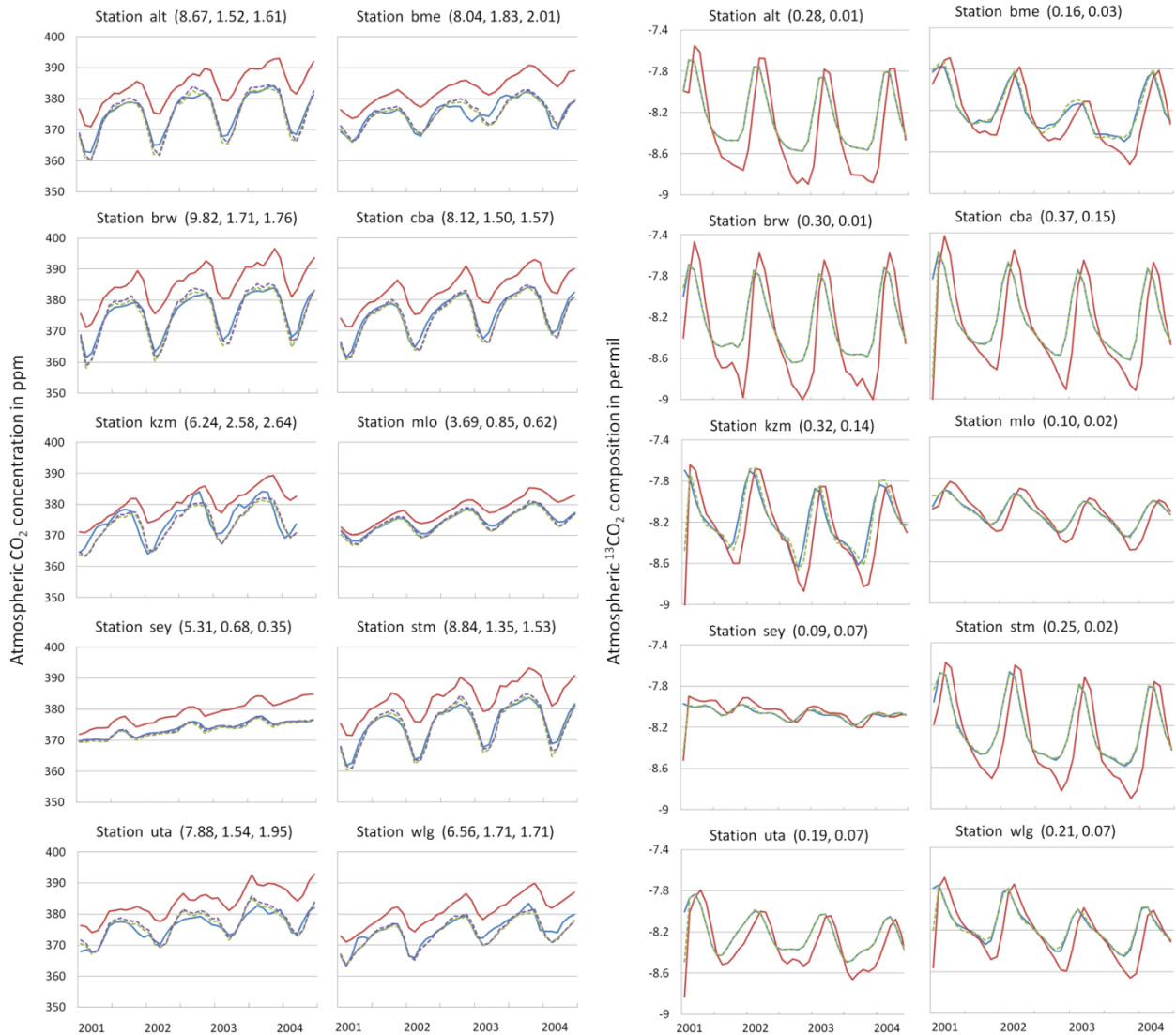
1292

1293 Figure 13. Left panel: comparison of CO_2 concentrations calculated using the prior flux (solid red)
1294 and from CO_2-only inversion (dashed purple) and joint inversion (dashed green) against observations
1295 (blue) at 10 randomly selected stations from different regions. The header of each plot indicates the
1296 station ID and the root mean square difference (RMSD) for the prior, joint and CO_2-only inversions
1297 against observations. Right panel: comparison of $^{13}CO_2$ composition from the prior (solid red) and
1298 joint inversion (dashed green) against observations (blue). The header of each plot indicates the
1299 station ID and RMSD of the prior and the joint inversion against observations.

1300

1301
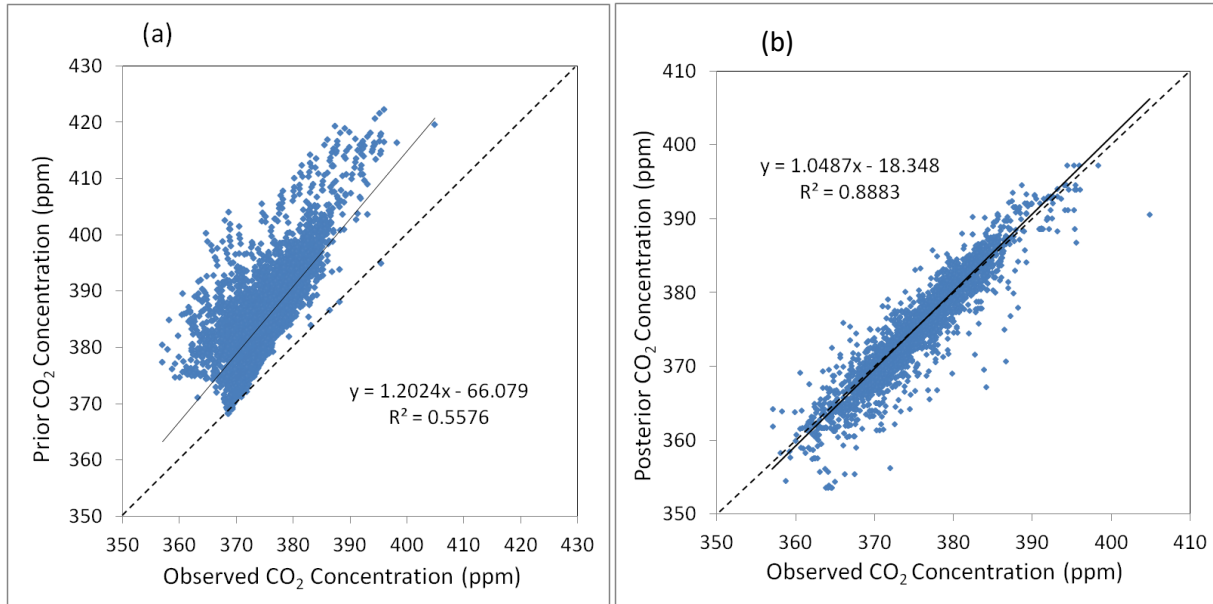
1302
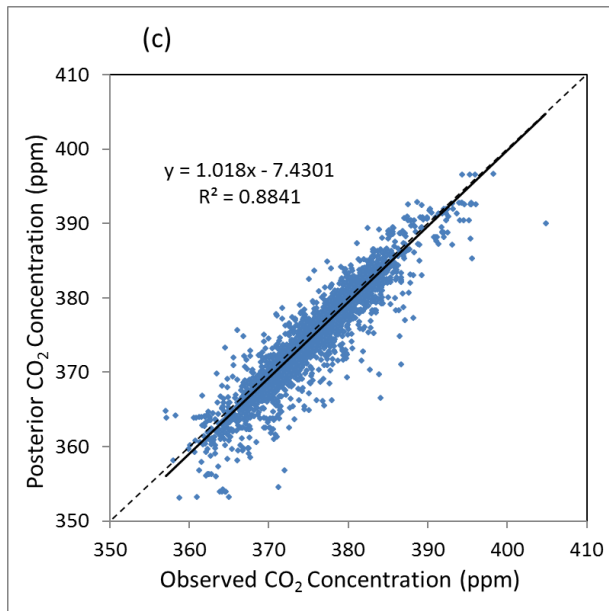
1303

1304

Figure 14. CO_2 concentrations from (a) prior, (b) posterior from the CO_2-only inversion, and (c) posterior from the joint inversion in comparison with observations. The prior concentration is obtained through transport modeling with prior CO_2 fluxes from the terrestrial ecosystems, oceans, fossil fuel emission, and biomass burning.

1309

1310

1311

1312
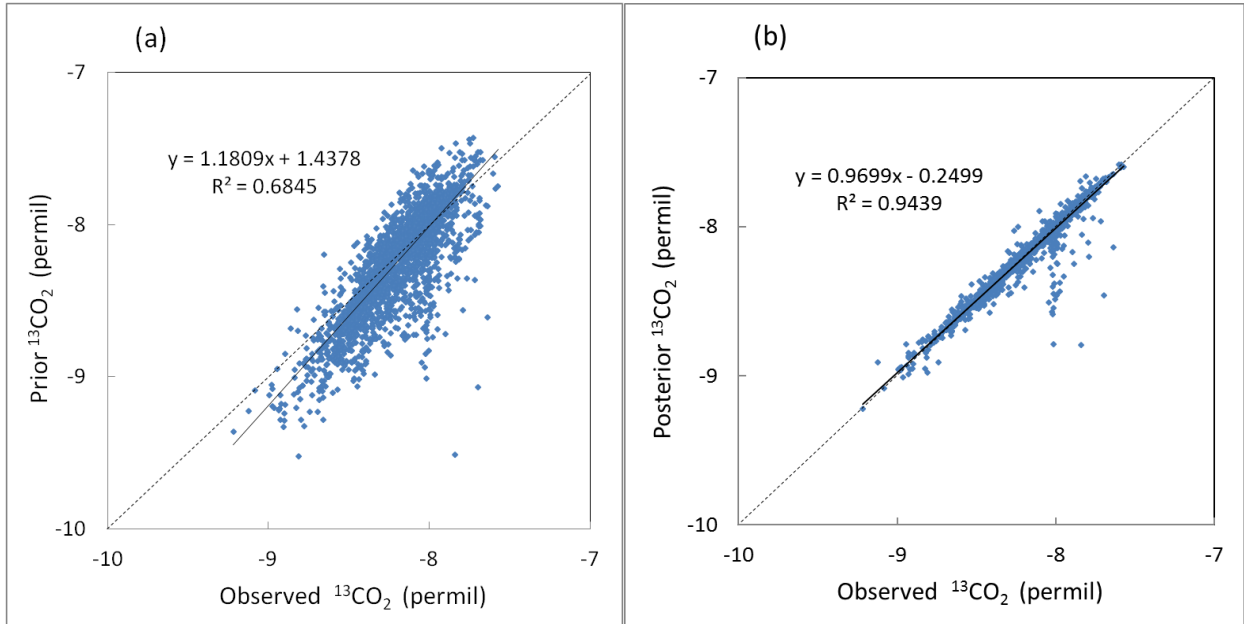
1313

1314

1315   Figure 15. Comparison of prior (a) and posterior (b) $^{13}CO_2$ compositions with observations. The prior

1316   composition is obtained through transport modeling with prior $^{13}CO_2$ fluxes from the terrestrial

1317   ecosystems, oceans, fossil fuel emission, and biomass burning, and the posterior composition is

1318   obtained with the CO_2-$^{13}CO_2$ joint inversion (Case I).

1319

1320

1321

1322

1323

1324